Control of innate olfactory valence by segregated cortical amygdala circuits

James R. Howe[1,2,3,9], Chung-Lung Chan[1,9], Donghyung Lee[1], Marlon Blanquart[1], James H. Lee[1], Haylie K. Romero[2,3,4], Abigail N. Zadina[5,†], Mackenzie E. Lemieux[6], Fergil Mills[6,††], Paula A. Desplats[3,4,7], Kay M. Tye[1,6,8], & Cory M. Root[1,*]

[1] Department of Neurobiology, University of California, San Diego, La Jolla, CA 92093, USA

[2] Neurosciences Graduate Program, University of California, San Diego, La Jolla, CA 92093, USA

[3] Department of Neurosciences, University of California, San Diego, La Jolla, CA 92093, USA

[4] Center for Circadian Biology, University of California, San Diego, La Jolla, CA 92093, USA

[5] Zuckerman Mind Brain Behavior Institute, Columbia University, New York, NY, 10027, USA

[6] Salk Institute for Biological Sciences, La Jolla, CA 92037, USA

[7] Department of Pathology, University of California, San Diego, La Jolla, CA 92093, USA

[8] Howard Hughes Medical Institute, La Jolla, CA 92037, USA

[9] These authors contributed equally

[†] Current affiliation: Department of Neuroscience and Behavior, Barnard College of Columbia University, New York City, NY 10027, USA

[††] Current affiliation: Department of Neurobiology, University of Utah School of Medicine, Salt Lake City, UT 84112, USA

* To whom correspondence should be addressed:

Cory M. Root, PhD
University of California, San Diego
9500 Gilman Drive
3119 Pacific Hall
La Jolla, CA 92093-0357
cmroot@ucsd.edu

Abstract

Animals exhibit innate behaviors that are stereotyped responses to specific evolutionarily relevant stimuli in the absence of prior learning or experience. These behaviors can be reduced to an axis of valence, whereby specific odors evoke approach or avoidance responses. The posterolateral cortical amygdala (plCoA) mediates innate attraction and aversion to odor. However, little is known about how this brain area gives rise to behaviors of opposing motivational valence. Here, we sought to define the circuit features of plCoA that give rise to innate attraction and aversion to odor. We characterized the physiology, gene expression, and projections of this structure, identifying a divergent, topographic organization that selectively controls innate attraction and avoidance to odor. First, we examined odor-evoked responses in these areas and found sparse encoding of odor identity, but not valence. We next considered a topographic organization and found that optogenetic stimulation of the anterior and posterior domains of plCoA elicits attraction and avoidance, respectively, suggesting a functional axis for valence. Using single cell and spatial RNA sequencing, we identified the molecular cell types in plCoA, revealing an anteroposterior gradient in cell types, whereby anterior glutamatergic neurons preferentially express *VGluT2* and posterior neurons express *VGluT1*. Activation of these respective cell types recapitulates appetitive and aversive behaviors, and chemogenetic inhibition reveals partial necessity for responses to innate appetitive or aversive odors. Finally, we identified topographically organized circuits defined by projections, whereby anterior neurons preferentially project to medial amygdala, and posterior neurons preferentially project to nucleus accumbens, which are respectively sufficient and necessary for innate attraction and aversion. Together, these data advance our understanding of how the olfactory system generates stereotypic, hardwired attraction and avoidance, and supports a model whereby distinct, topographically distributed plCoA populations direct innate olfactory responses by signaling to divergent valence-specific targets, linking upstream olfactory identity to downstream valence behaviors, through a population code. This suggests a novel amygdala circuit motif in which valence encoding is represented not by the firing properties of individual neurons, but by population level identity encoding that is routed through divergent targets to mediate distinct behaviors of opposing appetitive and aversive responses.

INTRODUCTION

Innate behaviors are ubiquitous across the animal kingdom, allowing specific sensory stimuli to yield stereotypical behavioral responses even in the absence of learning or past experience. These behaviors include feeding, fighting, fleeing, and mating, among others, and many can be simplified onto an axis of positive or negative valence representing approach and avoidance. Innate behaviors are the result of evolutionary selection, guiding initial behaviors that can be updated by future experiences. Given that innate behaviors are genetically hardwired, it is thought they should be mediated by simple circuits with specified connections between layers of the nervous system. Innate behaviors are common across sensory modalities but are especially prominent in olfaction, whereby diverse chemical signals, critical to survival and reproduction, must be quickly and robustly detected and processed, in the absence of prior experience. For instance, predator odors represent a potentially imminent threat and necessitate a quick, decisive, aversive response[1]. Conversely, innately appetitive odors represent potentially rewarding stimuli like food or heterospecifics, inducing attraction[2]. These odors comprise a small subset of perceptible chemical space, and the detection of specific odorants is both species-specific and under genetic control[3-5].

Valence is a fundamental perceptual feature of olfaction[6]. Motivational valence can be defined as seeking or avoiding specific stimuli, and it is observed across sensory stimuli in both innate and learned responses. Multiple circuit motifs have been proposed to mediate such valence responses[7]. In the simplest form, labeled line motifs segregate information from sensation to action throughout the nervous system. This has been observed in the taste and somatosensory systems, as well as hints of labeled lines in the olfactory system, where individual glomeruli are necessary and sufficient for innate responses consistent with this model[8-10]. Many circuits are organized along divergent path motifs, where a region receives the same sensory input but instead acts akin to a switchboard, processing and sorting its output to distinct downstream targets to convey positive or negative signals. This motif is most associated with the BLA and associated learning processes[7, 11]. Still other circuits contain opposing components motifs, in which opposing inputs target a single effector region to control the balance of one target. It remains unclear which, if any, of these generalized circuit motifs are present in the olfactory system.

Olfactory sensation begins with olfactory sensory neurons (OSNs) in the olfactory epithelium (OE) that express a single receptor, projecting to spatially stereotyped glomeruli in the olfactory bulb (OB). Postsynaptic mitral/tufted cells within the OB project in parallel to third-order olfactory areas, including the posterolateral cortical amygdala (plCoA). Unlike in other third-order olfactory areas, such as piriform cortex, projections from individual glomeruli from the OB to plCoA are spatially restricted and stereotyped, consistent with genetically hardwired circuits[12, 13]. Past work has demonstrated that plCoA is necessary and sufficient for innate olfactory responses, with spatially ordered labeling of responsive neurons via immediate early gene labeling[14]. However, other work suggests that there is no spatial organization to odor responses or valence encoding in plCoA[15]. Thus, a further investigation of plCoA organization is necessary to understand how this structure controls innate olfactory responses.

Distinct brain areas employ distinct coding strategies to represent information. Neuronal ensembles within all other major olfactory regions observed thus far, such as the anterior olfactory nucleus, OB, OE, olfactory tubercle (OT), piriform cortex (PIR), and tenia tecta all generally perform sparse population encoding of odor identity, despite the major differences in neuronal composition, organization, and function between the six regions[15-21]. On the other hand, ensembles within amygdala subnuclei, most notably the basolateral amygdala (BLA), instead tend to represent the valence of stimuli instead, with considerable heterogeneity based on a given population's projection target, molecular identity, and topography[11, 22]. A complete investigation of the encoding properties and organization of plCoA is needed to determine how innate olfactory valence emerges from this region.

To identify the plCoA circuitry that underlies innate attraction and avoidance to odor, we investigated multiple intersecting scales of organization, from single cell transcriptomes and spatial gene expression, to circuit mapping, manipulation, and physiology. First, we used 2-photon calcium imaging to find that plCoA ensembles encode odor identity, but not valence. Next, we identify a functional gradient in plCoA where activation of anterior and posterior neurons drives responses of opposing valence. Next, we characterized the cell types within plCoA, identifying novel, molecularly defined populations specific to each domain of plCoA, which are respectively sufficient and partially necessary for innate olfactory valence. Further, we perform comprehensive projection mapping to identify downstream projection targets of plCoA, identifying projections to the medial amygdala (MeA) and nucleus accumbens (NAc) that are enriched based on molecular and topographic identity. Finally, manipulations of neuronal ensembles projecting to these targets are sufficient and necessary to control innate olfactory valence responses. Together, these findings identify a novel topographically distributed circuit from plCoA to MeA and NAc that controls innate olfactory aversion and attraction, respectively, consistent with a hybrid model mixing features of labeled lines and divergent path circuit motifs.

RESULTS

Population Encoding of Odor Identity in plCoA

To better understand how plCoA circuitry mediates innate attraction and aversion, we first decided to examine the relationship between its spatial organization and odor-evoked activity. Prior analysis of immediate early gene expression following minutes-long odor exposure suggests that activity in the anterior and posterior domains of plCoA could respectively mediate innate aversive and appetitive odor responses[23]. However, *in vivo* electrophysiology with high-density electrode arrays found no evidence for spatial organization or valence encoding in plCoA[15]. These two studies propose contradictory models of plCoA encoding properties that are both plausible, given that the former is common in the extended amygdala and insular cortex[24], and the latter is ubiquitous across olfactory regions[18]. We speculated that technical differences could be responsible for these opposing findings. Immediate early gene labeling has low temporal resolution and likely requires a high amount of neural activity to activate gene expression. On the other hand, the recording sites in the latter study appear biased towards the middle of plCoA, and odor was given for 2 seconds in interleaved trials, whereas attraction and

avoidance responses have been measured on a minutes-long timescale[14, 25]. Although it is unclear when the valence of an odor is first perceived, we wondered if the apparent contradictions in these studies could be resolved by applying a longer odor delivery protocol that better matches the timescale of behavioral readouts and balances spatial and temporal resolution.

Therefore, we developed an approach to image neural activity in plCoA with a modified odor delivery schedule, expressing GCamP8s targeted towards either the anterior or posterior subsection of plCoA and implanting a gradient-index relay (GRIN) lens above to allow *in vivo* imaging of calcium transients via head-fixed two-photon microscopy (**Figure 1A-C, S1A-B**). We then examined calcium responses in these mice during a long odor exposure, where odors were presented repeatedly in 20-trial blocks for 5 seconds each in counterbalanced order (**Figure 1D**). We chose two odorants of each innate valence: the appetitive odors 2-phenylethanol (2PE) and peanut oil (PEA), the neutral odors heptanol (HEP) and isoamyl acetate (IAA), and the aversive odors trimethylthiazoline (TMT) and 4-methylthiazoline (4MT)[14]. In total, we recorded Ca^{2+} signals from 345 neurons across 13 mice.

First, we pooled anterior and posterior plCoA neurons together and performed hierarchical clustering of their trial-averaged responses to the 6 odors to categorize odor responses in an unbiased manner (**Figure 1E**). Consistent with the previous *in vivo* electrophysiology study, we found that the majority of plCoA neurons did not seem to selectively respond to odors of one valence group (**Figure 1E-F**). Across mice, a majority of plCoA neurons did not reliably respond to any of the six odors, and activity was sparse: only 34.5% of plCoA neurons responded to 1 of the 6 odors and 10% to 2 odors, while a much smaller portion of plCoA neurons responded to 3 or more odors (**Figure 1G**). Further, we found no significant relationship between the valence of odor and proportion of responsive neurons, and no difference in the proportion responsive to the different odors across anterior and posterior plCoA, suggesting a lack of bias in responsiveness to aversive or appetitive odors across the anterior-posterior axis (**Figure 1H**).

We next attempted to quantify valence encoding by calculating a valence score for each neuron by subtracting the average integrated aversive odor response from the average integrated appetitive odor response and dividing this resulting difference in valence by the integrated odor response ($V = \frac{\Sigma_{appetitive} - \Sigma_{aversive}}{\Sigma_{total}}$). Although the valence score was more negatively skewed amongst anterior neurons than posterior ones, there was no significant difference in their distributions, indicating that anterior and posterior plCoA neurons do not broadly encode opposing appetitive and aversive responses (**Figure 1I**). Given that the innate aversive and appetitive behaviors evolve over time in freely moving animals, we wanted to assess if odor responses changed between early and late trials. Using a moving window of 5 trials, we examined if the proportion of neurons with significant aversive or appetitive valence scores differed over time in anterior or posterior plCoA but found no significant interaction between time and imaging location (**Figure 1J**).

Repeated odor stimuli with the same odor was used to asses potential changes in odor representation that evolve over a time scale more consistent with our behavioral assay, but this

raises concerns about stability of odor delivery across trials and neuronal habituation. To address this, we first assessed the reliability of odor delivery and neuronal responses across trials. PID recordings of odor stimuli across trials revealed moderately stable delivery of all odorants (**Figure S1C,D**). Neutral odors were the least stable with a 29-39% decrease in PID detection between the first and last five trials, whereas the attractive and aversive odors decreased by 15-18%. Although the odors do not entirely deplete over time, these changes in odor concentration may affect physiological responses to odor. Next, neuronal response reliability was assessed by examining the frequency of neurons responding with a z score greater than 2 to each odor. With this criterion, the majority of neurons responded to less than half of the trials, while a subset responded to as many as 17/20 trials (**Figure S1E,F**). Using a less stringent criteria for responsiveness (z score > 1), more neurons appear to respond on more than half of the trials with a minority responding to all trials (not shown). It is noteworthy that these response probabilities are lower than that observed by Iurilli et al., using intermingled odor stimuli[15], indicating that repeated stimulus appears to cause to some habituation in odor response, which may also be partly due to a decrease in odor concentration. However, despite the weak reliability of individual neurons, the total number of responsive neurons in the population remained fairly consistent across trials (approximately 5-10%) after a decrease following the first two trials (**Figure 1K**). Thus, despite some changes in representation across trials, we do not see the emergence of valence and this doesn't appear to result from failure to deliver odor or stimulate neurons.

We further investigated odor encoding at the single neuron level using multinomial regression (MNR) 6-odor classifiers trained on single neuron data and found that they perform only marginally better than chance, suggesting that the majority of single plCoA neurons do not broadly encode discriminatory information about odor identity (**Figure 1K**). Across mice, only 43.1% have overall classification rates above the 95th percentile of shuffled controls, indicating that the majority of single plCoA neurons do not broadly encode discriminatory information about odor identity. Interestingly, when comparing the ranked sub-accuracies for single odors compared to shuffled controls, we found the discrepancy between data and shuffled controls to be accentuated in the 2 highest performing sub-accuracies (**Figure S1G**). Quantifying the proportion of neurons with sub-accuracies higher than the 95th percentile of the shuffled across biological replicates, we found that the decrease of sub-accuracies down the rank falls exponentially, rather than linearly (**Figure S1H**). This observation suggests that the individual neurons examined here have little information about the odors tested. This may seem surprising given that sparsely responsive neurons should carry highly specific information about odor identity. However, it is important to note that we are under sampling the large stimulus space (likely billions of odors), thus the neurons we sampled seem to carry little information about the limited stimulus space we tested. It is also possible that faint reliability dilutes the averaged signal used to decode from single neurons. Nonetheless, we do not find an enrichment for neurons specific to odors of valence.

Since we did not observe any evidence of valence encoding at the single neuron level, we next considered population level encoding. The plCoA neurons appear to primarily encode odor identity in a sparse manner much like the other higher-order olfactory areas, known to use

194 a population code. In contrast to the poor single neuron classification, SVMs trained on
195 population-level data vastly outperform the shuffled data, indicating good encoding of identity at
196 the population level (**Figure 1M,N**). We further used a confusion matrix to ask whether training
197 the classifier with a given odor could accurately predict the identity of another odor. In the matrix
198 each row corresponds to a predicted class and each column corresponds to the actual class
199 (**Figure 1O**). If the population level activity is similar between odor pairs, we expect the
200 confusion to be higher than less similar pairs. The output of a confusion matrix yields a
201 proportion of true class labels, whereby a high proportion indicates good prediction. We found
202 no difference between the confusion rates for intra-valence classification or inter-valence
203 classification, suggesting a lack of valence encoding at the population level (**Figure 1P**). The
204 similarity between inter-valence and intra-valence confusion was mirrored when quantifying the
205 range-normalized pairwise Euclidean distance across biological replicates (**Figure 1Q, S1I**).
206 Thus, plCoA appears to encode odor identity in a population code like other higher order
207 olfactory regions, with no apparent encoding of valence.

208 **A Functional Axis for Valence in plCoA**

209 Since we did not observe clear evidence for valence encoding, we considered other
210 organizational principles that could support appetitive and aversive behaviors. Spatial
211 organization for valence processing has been previously observed in the insular cortex and
212 BLA, whereby discrete subsections of the region contain neurons wired to preferentially signal
213 positive or negative valence[11, 22, 26]. Given plCoA's spatially-ordered afferent projections
214 from OB, we next hypothesized that plCoA circuitry could still be organized along the anterior-
215 posterior (AP) axis to support attraction and aversion. If true, it follows that activation of small
216 ensembles of neurons along the AP axis should generate behavioral responses along a
217 corresponding axis of valence. We tested this prediction by expressing channelrhodopsin
218 (ChR2) in subsets of neurons at different positions along this axis and photostimulating them
219 during behavioral testing in the previously established four-quadrant open field arena[14].

220 Based on cytoarchitecture, we parcellated plCoA into three domains: the anterior plCoA
221 (aplCoA), a two-layered region on the ventral surface lateral to the anterior cortical amygdala,
222 the posterior plCoA (pplCoA), a three-layered region on the ventrolateral surface lateral to the
223 posteromedial cortical amygdala, and a middle zone (mplCoA) between them (**Figure 2A**)[14].
224 To determine the potential relationship between position on the anterior-posterior axis of plCoA
225 and evoked behavior, we performed optogenetic stimulation at points along this entire axis,
226 expressing channelrhodopsin (ChR2) [27]and implanting fibers into each zone (**Figures 2B-C,**
227 **S2A**). Behavioral response was assessed using the four-quadrant open field assay, where mice
228 freely explored a chamber with or without stimulation, and approach or avoidance was scored
229 with a performance index measuring quadrant occupancy relative to chance, as well as the
230 mean distance to the corner port. Mice were tested for a 10 minute baseline period followed by
231 15 minutes of closed loop optogenetic stimulation (470nm, increasing from 1-10 Hz as the
232 mouse proceeds closer to the corner port) in one quadrant (**Figure 2D**)[14].

233 Throughout the trial period, we observed a negative linear relationship between the
234 anterior-posterior position of photostimulation site and the valence of the behavior. The amount
235 of time spent in the stimulated quadrant as well as the distance to the corner port varied in
236 ChR2, but not eYFP-infected mice, whereby responses shifted from appetitive to aversive as
237 stimulation became more anterior (**Figure 2E-F**). We grouped these responses to determine
238 whether these opposing responses were specific to the identified plCoA zones. We found that
239 photostimulation in aplCoA significantly reduced time spent in the 'on' quadrant and increased
240 the average distance to the corner port during the treatment period, indicating activation of
241 aplCoA neurons is aversive and leads to avoidance of the quadrant paired with stimulation
242 (**Figure 2G-I**). We also found the opposite was true in pplCoA, where stimulation in that zone
243 instead increased the time in the 'on' quadrant and decreased average distance to the corner
244 port, indicating pplCoA neuron activation instead is appetitive and leads to attraction to the
245 stimulation quadrant (**Figure 2J-L**). It is notable, that ChR2 labeling varied from as few as 100
246 to more than 500 neurons, without any correlation with behavior, and activation of these
247 domains is comparable to activation of sparse, odor labeled populations in past work[14], but a
248 threshold in the number of activated neurons remains to be determined.

249 We further examined the effects of anterior-posterior plCoA stimulation on other
250 behaviors to determine whether these effects were specific to appetitive and aversive
251 responses, or if they extended to other affective or motor phenomena. Using the elevated plus
252 maze, we found no change in anxiety based on open arm time or entries, across both the length
253 of plCoA or within either aplCoA or pplCoA (**Figure S3A-C, S3E-F, S3H-I**). In the open field test,
254 we similarly found no changes to thigmotaxis, based on time spent in corners of the open field,
255 or exploration, based on time spent in the center of the open field (**Figure S3K-M, S3EO-P,**
256 **S3R-S**). Further, locomotion remained constant during stimulation across both assays and the
257 entirety of plCoA (**Figure S3D, S3G, S3J, S3N, S3Q, S3T**). Together, these data suggest that
258 the effects of plCoA neuron activation across the entire anterior-posterior axis are specific to
259 approach and avoidance, with few other behavioral effects. Overall, we find that activation of
260 plCoA neurons is sufficient to drive behaviors of opposite valence in a topographically organized
261 manner, where aplCoA drives aversion and pplCoA drives attraction.

262 **Molecular Diversity of Transcriptomic plCoA Cell Types Along the Anteroposterior Axis**

263 Having identified a functional axis sufficient to produce approach and avoidance
264 behaviors (**Figure 2**) that does not appear to encode valence (**Figure 1**), we next considered if
265 the plCoA could be topographically organized by molecular cell type to support behaviors of
266 opposing valence. Thus, we sought to determine if there is an axis of molecular cell types along
267 the anteroposterior domains of plCoA. To investigate this phenomenon, we performed single-
268 nucleus RNA sequencing (snRNA-seq) to determine the cell type composition and its
269 relationship to the anterior-posterior axis of plCoA.[37] To simultaneously profile these cell types
270 and identify domain-specific patterns, we separately extracted tissue samples from aplCoA and
271 pplCoA by microdissection, verified accurate dissection by histology, and pooled qualifying
272 samples from the selected plCoA domain for each sequencing run (**Figure 3A, S4A-D**). We also
273 confirmed there were few region- or batch-specific differences in sequencing depth or nuclear

274 quality markers (**Figure S4E-M**). Clustering of sequenced nuclei by gene expression allowed
275 us to initially identify all major canonical neuronal and glial cell types in plCoA based on known
276 marker genes identified in past scRNA-seq studies (**Figure 3B-C**)[28, 29]. Neurons in plCoA are
277 80% glutamatergic, while 20% of neurons are GABAergic (**Figure 3D**). We also identified large
278 numbers of vascular leptomeningeal cells (VLMCs) and arachnoid barrier cells (ABCs), two
279 fibroblast-like meningeal cell types that interface with vasculature and form a barrier between
280 the brain and CSF, likely due to meningeal presence on the cortical surface during
281 extraction[28-31].

282 We further characterized the heterogeneity of glutamatergic and GABAergic neurons
283 within plCoA by re-processing and subclustering both major neuronal cell types. Within
284 glutamatergic neurons, we identified 14 distinct subtypes by gene expression, with largely
285 continuous variation between glutamatergic subtypes (**Figure 3E**). However, when examining
286 the relationships between these subtypes, we identified two broader groups of glutamatergic
287 neurons via hierarchical clustering, where subtypes within each group displayed a lower
288 Euclidean distance from one another in high-dimensional gene expression space (**Figure 3F**).
289 Each of these two broader groups had a marker for every type within either group, where the
290 larger Group 1 of glutamatergic neurons express *Slc17a7 (VGLUT1)*, and the smaller Group 2
291 expresses *Slc17a6 (VGLUT2)*. Within each of these glutamatergic groups, most observed
292 marker genes are non-canonical in the amygdala and cortex, suggesting unique glutamatergic
293 ensembles or patterns of gene expression within glutamatergic neurons in plCoA compared to
294 other regions previously described. Two subtypes did fall outside of either broad glutamatergic
295 group, varying in a more discrete manner than most plCoA glutamatergic neuron subtypes.
296 Interestingly, examination of data from the Allen ISH Atlas for their respective marker genes
297 *Etv1* and *Sim1* showed these two groups fall into adjacent regions outside of plCoA, where
298 Glut.Etv1 neurons localize to the posterior basomedial amygdala and Glut.Sim1 neurons
299 localize to the nucleus of the lateral olfactory tract (**Figure S5A-B**). However, gene expression
300 patterns for GABAergic neurons displayed an opposing form of heterogeneity, where subtypes
301 are more discrete, without broad groups linking related subtypes (**Figure 3G**). Marker genes for
302 GABAergic neurons are also more canonical than those in glutamatergic neurons, whereby
303 most GABAergic neurons in plCoA have interneuron-like identities, expressing canonical marker
304 genes such as *Vip, Sst,* and *Cck* (**Figure 3H**).

305 We hypothesized that differences in these populations' abundance could potentially be
306 responsible for the difference observed between different plCoA domains, and thus examined
307 potential domain-specific enrichment of certain cell types within plCoA. Visualization of these
308 nuclei with UMAP showed little clear region-specific structure for any major cell types (**Figure**
309 **4A**). This lack of structure was broadly confirmed quantitatively, where a few low-abundance
310 glial cell types showed significant domain-specific enrichment, but the high-abundance major
311 cell types did not (**Figure 4A-B**). In other brain areas, variations in the characteristics of
312 subgroups within major cell types are more pronounced than variations in the total numbers of
313 these major cell types, i.e. the balance of genes rather than balance of subtypes[32, 33].
314 Therefore, we examined abundance of differentially expressed genes (DEGs) between plCoA
315 domains for each major cell type. Here, we found that both major neuronal cell types had more

316 abundant DEGs than all major glial cell types (**Figure 4C**). Glutamatergic neurons DEGs
317 exceeded all other major cell types by a factor of 4, suggesting that differences between the
318 anterior and posterior domains are most likely to be observed via variation in glutamatergic
319 neurons.

320 Upon examination of domain-specific variation in plCoA glutamatergic neurons, we
321 initially observed a greater degree of domain-specific clustering in dimension-reduced space
322 (**Figure 4D**). Glutamatergic neuron subtypes correspondingly displayed domain-specific
323 enrichment, where more than half of glutamatergic neuron subtypes were significantly enriched
324 in either the anterior or posterior plCoA domain (**Figure 4E**). Upon closer examination, we found
325 that every glutamatergic subtype in the *VGluT2*-expressing Group 1 was enriched in anterior
326 plCoA, while *VGluT1*-expressing Group 2 subtypes are evenly distributed across fields or
327 biased towards the posterior, with one exception, Glut.Fign, which likely derives from the
328 aplCoA-adjacent cortex-amygdala transition area CxA, based on Allen ISH data of *Fign*
329 expression (**Figures 4F, S5A**). In contrast to glutamatergic neurons, we did not observe
330 significant plCoA domain-specific variation for any GABAergic neuron subtypes (**Figure S5D-E**).
331 We also found additional heterogeneity within glial cell types, including additional subtypes
332 within astrocytes and VLMCs (**Figure S5G-J, O-R**). We also observed domain-specific
333 divergence in gene expression for OPCs and astrocytes corresponding to domain-specific DEG
334 differences, though they did not correspond to any observable differences in subtype
335 enrichment (**Figure S5F, K-N**).

336 To confirm these findings and validate our snRNA-seq data, we directly examined spatial
337 RNA expression patterns. First, we used RNAscope labelling to examine the expression of
338 *VGluT2* and *VGluT1 in situ* in the plCoA, quantifying the number of nuclei expressing these
339 genes. We found that anterior plCoA had a much greater proportion of RNAscope-labelled
340 *VGluT*2+ nuclei (88%) than *VGluT*1+ nuclei (11%) compared to the rest of plCoA, where
341 *VGluT*1+ neurons predominate; posterior plCoA nuclei were almost entirely *VGluT1*+ (97%)
342 expressing (**Figure 4G**). It is noteworthy that these numbers were generally consistent with
343 those in our sequencing data.

344 The RNAscope patterns provide cellular resolution for two broadly distinct groups, but
345 lacks information on the broad distribution of more nuanced subtypes along the AP axis. Thus,
346 we next analyzed spatial gene expression in the plCoA from an existing Visium spatial
347 transcriptomics dataset that contained sagittal sections bisecting the plCoA along the midline
348 (Romero et al., in preparation; **Figure S5S**). Although the spatial resolution is limited to 55 μm
349 spots, this data set afforded an opportunity to test if the cell types we had identified by snRNA-
350 seq were distributed in a spatial gradient along the plCoA axis. We asked if the domain-specific
351 molecular cell type composition can be recovered directly from spatial information, without
352 depending on inference from dissection histology. All sections used were of similarly high quality
353 and did not display any clearly observable batch effects, with all but one having more than 100
354 spots covering the plCoA (**Figure S5T-W**). When clustering directly on spatial data, we
355 observed significant heterogeneity separating into three broad groups (**Figure 4H**). Like in
356 scRNA-seq, we found highly specific expression of *VGluT2* and *VGluT*1 to two of the three
357 broad spot groups (**Figure 4I**). When examining the spatial configuration of these groups, we

358 found the *VGluT*2-expressing group of clusters was in aplCoA, while the *VGluT*1-expressing
359 group was in pplCoA**,** with the third intermediate group corresponding to layer 1 (**Figure 4J-K**).
360 When computationally projecting transcriptomic cell type identities onto spatial data, we
361 observed that Group 1 glutamatergic neuron types would project onto pplCoA spots and Group
362 2 glutamatergic neuron types would project onto aplCoA spots, while negligible anteroposterior
363 bias could be observed when projecting GABAergic neuron types onto plCoA spots (**Figure 4L-**
364 **M**). It is important to note that this data set was collected from non-transgenic litter mate
365 controls in a study of APP23 Alzheimer's model. The mice were of the same genetic
366 background (C57BL/6J) but a different age as our sequencing specimens. Thus, these data
367 confirm the robustness of our findings from sn-RNA-seq and in situ hybridization, and further
368 demonstrate that plCoA contains a diverse population of numerous neuronal subtypes that vary
369 along a gradient. Whereas glutamatergic neuron subtypes vary significantly along the
370 anteroposterior axis, such that aplCoA-enriched subtypes express *VGluT*2 and pplCoA-enriched
371 subtypes express *VGluT1.*

372 **Molecularly Defined plCoA Glutamatergic Neuron Populations Contribute to Approach**
373 **and Avoidance Behaviors**

374 Given this spatial distribution bias of plCoA$^{VGluT2+}$ neurons into aplCoA and plCoA$^{VGluT1+}$
375 neurons into pplCoA, we further hypothesized that these glutamatergic neuron subtypes could
376 be responsible for the opposing valence responses observed during topographic plCoA
377 stimulation (**Figure 2**). If distinct molecular cell types mediate opposing valence, the
378 topography-independent activation should elicit opposing responses. To investigate this, we
379 expressed ChR2 in a non-spatially-biased, cell type-specific manner using a Cre-dependent
380 viral construct in *VGluT2::Cre* and *VGluT1::Cre* transgenic mice, targeting AAV-DIO-hSyn-ChR2
381 into mplCoA and implanting optic fibers above the injection site (**Figures 5A-B, S2B**). Using the
382 prior four-quadrant open field task, we found that photostimulation of plCoA$^{VGluT2+}$ neurons
383 significantly reduced time spent in the 'on' quadrant and increased the average distance to the
384 corner port during the treatment period, indicating that activation of plCoA$^{VGluT2+}$ neurons is
385 aversive and leads to avoidance of the quadrant when paired with stimulation (**Figure 5C-E**). In
386 contrast, photostimulation of the plCoA$^{VGluT1+}$ neurons instead increased the time in the 'on'
387 quadrant and decreased average distance to the corner port, indicating plCoA$^{VGluT1+}$ neuron
388 activation is appetitive and leads to attraction to the stimulation quadrant (**Figure 5C,F-G**).
389 These data suggest that the divergent domain-specific valence effects of plCoA activity could be
390 due to the divergent molecularly defined neuronal ensembles predominant in each
391 topographical field of plCoA.

392 Next, we sought to determine whether these two glutamatergic populations are
393 respectively required for innate attraction and aversion to odor. We used the above transgenic
394 mouse lines to drive expression of a viral Cre-dependent hM4D(Gi) construct to selectively
395 inhibit these neurons' activity via chemogenetics [34] (**Figure 5I, Figure S6A-C**). We
396 administered clozapine-N-oxide (CNO) or a vehicle control and used the four-quadrant open
397 field assay[14] to assess their behavioral responses to the innately-attractive 2PE or the
398 innately-aversive TMT to determine the difference in the magnitude of temporally-
399 counterbalanced valence responses when the respective populations are chemogenetically

400 silenced. These two odors were chosen because they most robustly drive approach and
401 avoidance, and were used in our previous work demonstrating the role of plCoA in innate
402 responses.

403 We observed that both transgenic mouse lines displayed attraction and aversion to 2PE
404 and TMT following administration of the vehicle control. Inhibiting plCoA$^{VGluT2+}$ neurons by CNO
405 administration did not affect the response to either odorant (**Figure 5J-Q**). However, inhibiting
406 plCoA$^{VGluT1+}$ neurons abolished the attraction to 2PE, without affecting aversion to TMT (**Figure**
407 **5J-Q**). In other words, neither group of plCoA glutamatergic neurons are selectively required for
408 TMT aversion, but plCoA$^{VGluT1+}$ neurons are required for attraction to 2PE. Further, silencing of
409 either population did not lead to any broader non-olfactory behavior effects as measured by the
410 EPM and OFT assays, including anxiety, exploration, and motility, showing the effects of
411 silencing these neurons are likely limited to valence and/or olfaction alone, instead of
412 exploratory or defensive behaviors (**Figure S5C-N**). The necessity of plCoA$^{VGluT1+}$ neurons for
413 2PE attraction, combined with their ability to drive approach responses with stimulation indicates
414 that these of plCoA$^{VGluT1+}$ neurons signal attraction. However, plCoA$^{VGluT2+}$ neurons, although
415 sufficient to drive aversion, are not necessary for aversion. Further work is required to identify
416 the a molecularly defined population for aversive responses.

417 **A Topographic Organization of plCoA Defined by Limbic Projection Targets**

418 The anatomical connectivity of the plCoA has not yet been defined in the mouse brain.
419 Further, we posited that the differences in necessity of plCoA cell types could be due to
420 divergent downstream connections instead of divergent molecular features, which may partially,
421 but not completely overlap. Thus, we next sought to identify distinct downstream outputs of
422 plCoA that could explain the bidirectional valence effects of its topography. We first
423 characterized the downstream outputs of plCoA by co-injecting the anterograde viral tracer
424 AAV-DIO-hSyn-mRuby2-T2A-synaptophysin-EGFP and a constitutive AAV-Cre virus into
425 mplCoA to label presynaptic terminals with EGFP (**Figure S7A-B**). We observed a high amount
426 of terminal fluorescence within plCoA itself, suggesting the presence of recurrent connections
427 within the region (**Figure S6B**). In addition, we observed long-range projections to a diverse set
428 of regions, including surrounding extended amygdala subregions, such as MeA and the
429 amygdalo-hippocampal transition area (AHi), regions controlling valence and emotion, like the
430 NAc and the bed nucleus of the stria terminalis (BNST), and regions involved in olfactory
431 processing, primarily PIR and OT (**Figure 6A-D**).

432 Among these outputs, we hypothesized that the NAc and the MeA could be responsible
433 for the behavioral divergence between anterior and posterior plCoA, given their known
434 involvement in reward expectation and aversion, respectively[35, 36]. We sought to confirm
435 these differences using retrograde tracing from MeA or NAc, where red retrobeads were
436 injected into MeA or NAc and labeled neurons were quantified along the anterior-posterior axis
437 (**Figure 6E**). For both downstream targets, we observed opposing gradients of retrobead
438 projector labeling throughout the entire plCoA anteroposterior axis (**Figure 6F**). MeA-projecting
439 neurons are enriched in aplCoA, and NAc-projecting neurons are enriched in pplCoA, with each
440 having a frequency of around chance level in mplCoA (**Figure 6G**). Further, the majority of

441 labeled plCoA-MeA projection neurons were in aplCoA, while the majority of labeled plCoA-NAc
442 projection neurons were in pplCoA (**Figure 6H**). To further confirm the spatial bias in projection
443 targets, we performed anterograde tracing from the aplCoA and pplCoA by injecting viruses
444 expressing either eYFP or mCherry into either domain of plCoA in a counterbalanced manner
445 (**Figure S7D-E**). Anterograde projection strength from aplCoA and pplCoA revealed that
446 projections to MeA were most dense from aplCoA, and projections to NAc were most dense
447 from pplCoA (**Figure 6I-K**). The aplCoA sent a significantly higher proportion of its projections to
448 MeA than pplCoA, whereas pplCoA sent a significantly higher proportion of its projections to
449 NAc (**Figure 6L**).

450 We reasoned that the topographical sufficiency we observed (**Figure 2**) could be
451 explained by cell type-specific divergence in projection target, whereby the topographical biases
452 in downstream targets are recapitulated by their underlying molecular cell type. To determine
453 the relationship between cell types and projection targets, we injected Cre-dependent eYFP into
454 mplCoA in *VGluT2::Cre* and *VGluT1::Cre* transgenic mice, targeting the middle to ensure
455 differences result from cell type, instead of simply redundant topography (**Figure S7F-G)**.
456 Interestingly, the relationship was not as simple as one cell type, one primary projection target.
457 Rather, both cell types project to both structures in different proportions. The plCoA$^{VGluT2+}$
458 neurons primarily project to MeA with a significant bias for that target over NAc, while
459 plCoA$^{VGluT1+}$ neurons project to both MeA and NAc, with a statistically insignificant bias toward
460 NAc (**Figure 6M,P**). These findings demonstrate that NAc primarily receives projections from
461 plCoA$^{VGluT1+}$ neurons, whereas the MeA receives input from both populations. Moreover,
462 projection of both cell types to the MeA may explain why neither *VGluT* population was
463 selectively required for innate aversion (**Figure 5J-Q**).

464 Given that both cell types project to both MeA and NAc, we sought to determine the
465 extent of collateralization in neurons composing the two pathways. To test whether plCoA-MeA
466 and plCoA-NAc projection neurons also project to multiple or overlapping downstream targets,
467 we employed a combination of retrograde Cre and Cre-dependent anterograde tracer viral
468 vectors. A retroAAV-hSyn-Cre-mCherry virus was into either MeA or NAc, and AAV-DIO-ChR2-
469 eYFP was injected into plCoA to label outputs of MeA- or NAc-projecting neurons (**Figure 6Q-R,**
470 **S7H-I**). We focused on MeA and NAc, as well as the ancillary primary downstream targets
471 implicated in valence or olfaction. We found different collateralization patterns for both
472 populations, where NAc-projecting neurons did not collateralize to MeA, but very strongly
473 collateralized to OT. In contrast, MeA-projecting neurons minimally collateralized to NAc and
474 most strongly collateralized to pmCoA (**Figure 6S-T**). Notably, neither projection of interest
475 significantly collateralized to the other. These data indicate that plCoA-MeA and plCoA-NAc
476 projection neurons are largely non-overlapping, spatially biased populations that output to
477 different downstream subnetworks.

478 **Projections from plCoA NAc to MeA and Respectively Mediate Attraction and Aversion to**
479 **Odor**

480 The topographic separation of MeA- and NAc-projecting neurons are consistent with a
481 model of divergence valence that could support the observed topographic divergence

482 behaviors. To investigate the behavioral contributions of these projections, we first determined
483 whether the neurons projecting to the MeA and NAc are able to drive behavior with optogenetic
484 stimulation. We expressed ChR2 in a non-spatially biased manner by injecting AAV-hSyn-ChR2
485 into mplCoA, and we placed an optic fiber above MeA or NAc for selective optogenetic
486 stimulation at plCoA axon terminals (**Figure S1C**). We found that photostimulation of the plCoA-
487 MeA circuit in the four-quadrant open field task significantly reduced time spent in the 'on'
488 quadrant and increased the average distance to the corner port during the treatment period,
489 indicating activation of the plCoA-MeA circuit is aversive and leads to avoidance of the quadrant
490 paired with stimulation (**Figure 7A-D**). The opposite was true for the plCoA-NAc projection,
491 where stimulation in that zone instead increased the time in the 'on' quadrant and decreased
492 average distance to the corner port, indicating activation of the plCoA-NAc circuit is instead
493 appetitive and leads to attraction to the stimulation quadrant (**Figure 7B,E-F**). We next asked if
494 the effects of stimulating these circuits affected other non-valence behaviors by testing the mice
495 in the EPM and OFT. Using the EPM, we found no change in anxiety based on open arm time
496 or entries when stimulating either projection to the MeA or NAc (**Figure S8A-C,E-F,H-I**).
497 Similarly, stimulation in the OFT did not cause any change to thigmotaxis, based on time spent
498 in corners of the open field, or exploration, based on time spent in the center of the open field
499 (**Figure S8K-M,O-P,R-S**). Further, locomotion remained constant during stimulation across
500 both assays (**Figure S8D, S8G, S8J, S8N, S8Q, S8T**). These data indicate that the divergent
501 projections from plCoA to the MeA and the NAc are capable of driving valence-specific
502 behaviors without modulating anxiety.

503 Finally, we sought to determine whether plCoA-MeA or plCoA-NAc projections are
504 necessary for the expression of odor-evoked appetitive or aversive behaviors. To target these
505 projection neurons for chemogenetic silencing, we injected a retroAAV bearing an hSyn-EBFP-
506 Cre construct into MeA or NAc, along with an AAV in plCoA bearing a Cre-dependent hM4D(Gi)
507 construct (**Figure 7G,H**). We then tested the innate responses of these animals to 2PE or TMT
508 in the four-quadrant assay following administration of CNO or a vehicle control, as above.
509 Inhibition of plCoA-NAc projection neurons abolished innate attraction to 2PE without having
510 any effect on aversion to TMT (**Figure 7I-L**). Conversely, inhibition of plCoA-MeA projection
511 neurons had no effect on innate 2PE attraction, but significantly decreased the aversion to TMT
512 (**Figure 7M-P**). Silencing these neurons had no effect in the EPM and OFT assays, indicating
513 the effects of silencing these neurons are limited to valence or olfaction, and not anxiety or
514 exploration (**Figure S8M-X**). Thus, plCoA-MeA projection neurons are necessary and sufficient
515 for innate aversion to TMT, whereas plCoA-NAc projection neurons are necessary and sufficient
516 for innate attraction to 2PE.

517

518 **DISCUSSION**

519 **Topographic Organization of Valence in plCoA**

520 The neural circuits mediating innate attraction and aversion to odor have not been fully
521 defined. Here, we have advanced our knowledge of the circuitry underlying innate olfactory
522 behaviors by defining its activity and organization within plCoA and further extending the innate
523 olfactory pathway from a third order olfactory brain area to limbic structures involved in

motivational valence. We have identified a novel functional axis for valence with the plCoA that is defined by histologically and functionally distinct domains along the anteroposterior axis. We have characterized odor encoding in plCoA, identifying a sparse population code for identity of an odor, but not its innate valence, consistent with previous finding[15]. We have also determined the composition of molecular cell types in plCoA and identified spatially biased populations enriched within each domain, which we find sufficient to drive their respective domain-specific behaviors, though only partially necessary for their functions in olfaction. Moreover, we identified the outputs of plCoA and quantitatively characterized the relative anatomical strength of each, as well as how it relates to plCoA topography and domain-specific molecular cell types, demonstrating that neurons projecting to the MeA and NAc are topographically and molecularly biased. Finally, we demonstrate that neurons projecting to the to the NAc and MeA are capable of driving approach and avoidance responses, and loss of function experiments demonstrate that the neurons projecting to the NAc or MeA are selectively support innate olfactory attraction and avoidance, respectively. Thus, plCoA is composed of dissociable, spatially segregated ensembles for divergent valence, defined by their downstream projection target. Though it remains to be determined how broadly these neurons contribute to the valence of other odors.

Spatial organization for features of sensory stimuli is common in sensory cortex, and has been previously proposed as fundamental to sensory processing[37]. Visual cortex is topographically organized by retinotopic locations in space, somatosensory cortex contains a map of the body, auditory cortex has a crude tonotopic organization by frequency, and gustatory cortex is segregated by taste qualities[24, 38-40]. However, topographic organization by perceptual feature has not been observed in the olfactory system, which has been attributed to the high dimensional nature of olfactory information[18]. Our findings identify a topographically organized divergence motif for valence in plCoA, where activation of aplCoA evokes aversive behavioral responses, and activation of pplCoA evokes attractive behavioral responses, with a graded transition between the two domains. This is consistent with prior studies implicating a spatial organization to inputs from the OB to plCoA, where glomerulus-specific anterograde tracing from OB shows specific glomeruli send fibers to invariant, densely clustered, anatomically distinct locations within plCoA, and retrograde tracing from plCoA shows that upstream glomeruli are spatially biased within OB[41] and closer examination reveals that OB input can co-vary with plCoA anteroposterior position. Interestingly, spatial segregation of divergent features is present elsewhere in olfaction as well, although not by perceptual feature. Olfactory sensory receptors display stereotyped spatial organization within zones of the olfactory epithelium, with a corresponding spatially-stereotyped glomerular topography in OB[19, 42-44]. Further, these topographic domains in OB have functional relevance, where region-specific OB manipulations selectively alter different olfactory behaviors[25, 45]. However, the piriform cortex generally lacks apparent spatial organization or spatial patterning for odor responses[18]. Thus, the topographical organization of valence observed here in plCoA represents one of the first descriptions of these spatial patterns occurring in central olfactory areas.

Topographic gradients for appetitive and aversive responses have been observed in other limbic regions, including the BLA[22], the medial amygdala for innate social behaviors[46],

Drosophila dopaminergic mushroom body neurons for olfactory learning[47], and the gustatory insular cortex for taste[48]. Our results extend this phenomenon of spatially segregated neurons for valence into a less well-described amygdala nucleus, and suggest that it could serve as a potential common motif within the limbic system to organize motivational information, especially for innate behaviors, which require stereotyped neurocircuitry. We believe a model whereby aplCoA and pplCoA are parts of the same region with similar underlying composition, but with a gradual change in the factor that defines the valence output for a given part of the gradient would best explain the underlying gradient-like effect on approach and avoidance. We considered two such organizational principles underlying this topography: molecular cell types and projection targets. We found that broad divisions of cell types by *VGluT*2 and *VGluT1* did not fully define valence, though more specific subtypes could be responsible. Our results indicate that the projection targets of plCoA neurons are a fundamental feature for imparting valence on this circuitry.

Molecular Cell Types in plCoA Segregate Topographically and Support Behaviors of Divergent Valence

While examining the cell types composing plCoA, we noticed numerous notable, novel features. First, despite its small area (~1.04 mm^3 and ~170,000 cells), plCoA displays remarkable diversity, hosting dozens of distinct, robustly separable cell types[49]. The plCoA appears to have multiple domains positioned at the transition between disparate brain tissue types. Interestingly, the high-dimensional structure of molecular variation differs between glutamatergic and GABAergic neurons. Glutamatergic molecular variation within plCoA is continuous, with two broadly nested groups generally marked by either *VGluT2* or *VGluT1* along with one or more additional marker gene(s)*,* though it should be noted that expression of the two broad glutamatergic markers is not necessarily mutually exclusive and a few low abundance “transition” cell types can express both. This leaves open the possibility that a more specific cell type could be necessary for aversion, given that this necessity for this behavior did not map onto either broad molecular cell type. In contrast, molecular variation in GABAergic neurons is far more discretized, with ensembles expressing one of a few well-characterized interneuron markers found throughout the brain, such as *Sst, Vip,* and *Pvalb*, among others. This is consistent with other studies in neocortex, hippocampus, and subiculum that find similar patterns of variation, whereby variation within glutamatergic neurons is more continuous than in GABAergic neurons[32, 50]. In this manner, we find the continuous gradient-like structure of valence in plCoA is recapitulated with gradient-like variation in glutamatergic neuron gene expression in plCoA.

In these molecular datasets, we further observed specific differences in cell type enrichment within aplCoA and pplCoA within glutamatergic neurons, but not GABAergic neurons or glia. Within plCoA, *VGluT2*+ neurons are enriched in aplCoA and *VGluT1*+ neurons are enriched in pplCoA, though there is gradient-like intermingling of populations, especially toward the middle of plCoA, and all glutamatergic neuron types are present, albeit with high variability along the anteroposterior axis. This molecularly defined order suggests a programmed organization, rather than stochastically distributed populations within the region, especially given that its boundaries match the domains previously identified based on behavior

609 and histology[51]. This phenomenon also broadly matches observations in the neocortex,
610 hippocampus, and subiculum, where glutamatergic neurons across subdivisions molecularly
611 diverge to a greater degree than GABAergic neurons or glia, albeit across a correspondingly
612 greater area than within plCoA, which is generally accompanied by distinct morphological and
613 electrophysiological properties broadly corresponding to these transcriptomic differences[32, 33,
614 50, 52]. Spatial segregation of molecular cell types is also observed within deeper brain regions
615 including BLA, thalamus and habenula, and these molecular differences are also accompanied
616 by extended phenotypic differences[22, 53-55]. Investigation of such properties held in common
617 and diverging within and between *VGluT2*+ and *VGluT1*+ glutamatergic neuron types could also
618 serve to further define the local neurocircuitry and information processing dynamics within
619 plCoA and along its anteroposterior axis.

620 Interestingly, few if any populations within plCoA are clearly separable from most of the
621 regions surrounding it (e.g. piriform cortex, basomedial amygdala, and MeA) based on primary
622 marker gene identity. Instead, plCoA ensembles seem to be defined by the interplay of all three
623 regions within the same tissue. The predominance of populations resembling different regions
624 does appear related to this anteroposterior organization, though, where *VGluT2*+ neurons
625 predominate in both aplCoA and MeA, and more specific marker genes like *Meis2* are
626 expressed in both regions as well[56]. Conversely, *VGluT1*+ neurons predominate in both
627 pplCoA and piriform cortex, and the major marker genes like *Satb2* are similarly expressed in
628 both regions[57]. Such phenomena are also consistent with general characterizations made in
629 whole-brain molecular taxonomies, which divide plCoA along its axis, grouping aplCoA with
630 MeA and pplCoA with paleocortex[58-60]. It would be misleading to characterize plCoA
631 populations as mere extensions of surrounding populations into an adjacent region, though.
632 *VGluT1*+ neurons from the cortex-amygdala transition zone are also present in the dataset and
633 are continuously separable from *VGluT1*+ plCoA neurons based on the expression of marker
634 genes like *Fign*. Instead, plCoA may itself be a transition region, given that such a relationship
635 with its neighboring regions is very similar to that of the amygdalostriatal transition area, one of
636 the only transition regions to undergo high-resolution molecular profiling[61]. Given such
637 commonalities between these two putatively dissimilar regions, molecular characterization of
638 additional transition regions could potentially uncover similar organizational motifs, especially if
639 compared with adjacent regions of interest, and allow for a much more in-depth exploration and
640 characterization of the boundaries and transitions between proximally located, distantly related
641 brain regions.

642 These broad molecular groups of glutamatergic cell types themselves do not completely
643 explain valence in the plCoA. While aplCoA-enriched *VGluT2*+ neurons are sufficient to drive
644 aversion and pplCoA-enriched *VGluT1*+ neurons are sufficient to drive attraction, as would be
645 predicted from the valence responses evoked from each anterior-posterior domain enrichments,
646 it might be expected that these populations would also be necessary for the respective odor-
647 evoked valence. However, only *VGluT1*+ neurons are necessary for 2PE attraction, whereas
648 the *VGluT2*+ neurons were not required for aversion to TMT. Given that the plCoA is necessary
649 for TMT aversion, it is unlikely that such a difference is due to additional redundant function
650 within other regions for TMT aversion[14]. Rather, although *VGluT2*+ neurons likely contribute
651 to aversion, other populations within the region not expressing the marker gene could also

652 contribute to the behavioral response. Thus, although these two broad glutamatergic groups can
653 drive innate responses of valence, the *VGluT2+* population doesn't fully represent the
654 population that control aversive responses, which is supported by other findings presented here
655 showing that both *VGluT2+* and *VGluT1+* neurons project to MeA, while the projection to NAc is
656 almost entirely composed of *VGluT1+* neurons. Regarding more specific molecular cell types, it
657 could be possible that only a subset of *VGluT1+* neurons are required for 2PE attraction.
658 Similarly, the neurons required for TMT aversion could be marked by a gene orthogonal to the
659 observed *VGluT*2/*VGluT*1gradient, and genetic access to olfactory aversion could potentially be
660 established by investigating these more sparsely expressed marker genes. In both cases,
661 though, further investigation into these other cell types would enhance our understanding of
662 both plCoA and innate olfactory valence and allow more precise manipulations in the future.

663 **Downstream Projection Targets of plCoA Divergently Control approach and avoidance**

664 In this work, we perform the first comprehensive characterization of plCoA's downstream
665 outputs in the mouse brain. These outputs are dominated by regions generally involved in
666 valence and emotion, such as the NAc, BNST, MeA, BLA, and other amygdalar nuclei, or
667 olfactory areas, such as the pmCoA, OT, and PIR. These outputs are consistent with a role for
668 plCoA in motivational valence for odor. The plCoA also appears to form numerous intra-regional
669 connections, where a significant proportion of synapses formed with other neurons are within
670 the region itself. This raises the possibility that plCoA is not simply a feedforward relay but
671 performs local recurrent processing as well. Recurrent networks in other sensory systems
672 expand the dimensionality of encoding schemata and incorporate additional features to
673 generate mixed, continuously updating representations of relevant information[62]. This raises a
674 number of interesting questions regarding information processing within plCoA. For instance,
675 how does odor representation change based on differences in experience and internal state?
676 Further explorations of information transformation and encoding within plCoA will enrich our
677 understanding this region.

678 The NAc and MeA are interesting downstream targets given their known relationships to
679 appetitive and aversive responses, respectively. NAc has historically been critical to the
680 manifestation and processing of reward and motivated behaviors, though this view has been
681 expanded and made more nuanced with a recent focus on action selection[63]. On the other
682 hand, MeA has been linked to defensive and stress-related behaviors in response to aversive
683 stimuli. MeA has also been specifically linked to olfactory aversion in past studies, as TMT has
684 previously been shown to activate the MeA[64], which is necessary for TMT-induced defensive
685 behaviors[35], though the upstream circuits and processing were not yet investigated. These
686 circuits are also notable regarding other features of plCoA spatiomolecular organization, as the
687 projections to the downstream regions of interest are the two that diverge to the greatest extent
688 between aplCoA and pplCoA, and between plCoA$^{\mathrm{VGluT2+}}$ and plCoA$^{\mathit{VGluT1+}}$ glutamatergic
689 neurons. Given the relationship between spatiomolecular patterning and the simple wiring and
690 organizational rules used to structure innate circuits it would be interesting to investigate the
691 plCoA through the lenses of development and genetic variation. These intersect in recent
692 discussions of genetic bottlenecking, where the genome encodes general rules for circuit
693 organization and development that nevertheless yield specific responses to specific stimuli[65].

694 Such networks have numerous theoretical advantages, such as reduced information
695 requirements and higher performance at criterion, providing a conceptual basis for why
696 spatiomolecularly stereotyped circuits yield innate behaviors, and why these innate behaviors
697 are adaptive in naturalistic settings[65-67].

698 **Neuronal Activity in plCoA Encodes Odor Identity Via Sparse Population Code**

699 The plCoA receives spatially-ordered inputs and has a cell-type-specific topographical
700 organization with divergent outputs that mediate approach and avoidance responses. This
701 anatomical organization is consistent with either labeled-line or divergent paths motifs, though
702 precise connectivity from OB has not yet been described. However, labeled line coding motif is
703 not apparent in neural activity, but instead there is a sparse population code for odor identity
704 with no apparent valence-specific responses, indicating that the plCoA cannot function as a
705 pure labeled-line relay. Moreover, the absence of valence encoding is distinct from that seen in
706 other divergent path motifs, suggesting the plCoA represents a different circuit model for
707 valence.

708 We were surprised to find that despite a robust organization of plCoA cell types and
709 projections that support approach and avoidance behaviors, the neurons do not appear to
710 encode appetitive and aversive responses at the single neuron or population level. However,
711 when put in the context of the olfactory system, these results are less surprising. Sparse,
712 distributed population encoding appears to be a general feature of all olfactory regions observed
713 thus far, regardless of their specific structure or computational function within olfaction. In the
714 OE, OSNs expressing a single receptor will bind multiple odorants and establish odor identity
715 through a combinatorial code.[21,23] In the OB, axon terminals from OSNs expressing the same
716 receptor converge into specific stereotyped glomeruli, where mitral/tufted cells (M/T) then
717 transmit this information to third-order olfactory regions. Both layers represent the odor identity
718 via a sparse population code in a spatially-distributed manner[19, 68]. The primary olfactory
719 cortex further represents odor identity through sparse, spatially distributed combinatorial
720 population activity in a similar manner[18]. The OT, a striatal region primarily composed of *Drd1*-
721 or *Drd2*-expressing medium spiny neurons, also broadly represents odor identity across both
722 cell types, despite their opposing roles elsewhere in striatum, and a contribution to learned
723 hedonic value is currently debated[20, 69]. Although direct comparisons of olfactory regions find
724 some differences in features like sparsity, clustering, or correlation structure, these are generally
725 reported as differences in degree, not in kind. Given the remarkable similarity in encoding
726 between these structurally and functionally distinct regions, it logically follows that an olfactory
727 region with amygdalar structure would follow similar population encoding principles. Indeed,
728 were plCoA to predominantly encode stimulus valence in a manner akin to other amygdalar
729 regions, it would reflect a greater divergence from olfactory coding principles than what we
730 observe. Instead, the olfactory encoding scheme employed by plCoA reveals a framework for
731 valence encoding that is distinct from that in the extended amygdala.

732 How does innate valence arise from a population code imposed on stereotyped
733 circuitry? One possibility is that the valence of an odor is defined by the proportion of NAc and
734 MeA-projecting neurons activated, mixing features of divergent paths and opposing components

motifs. In this model a given odor should activate some balance of NAc and MeA projecting neurons and the proportional balance determines the behavioral response (**Figure 8A**). If true, one should be able to predict the valence of the odor by recording from a large sample of these projection-defined neurons. A similar model has also been proposed in the OB[70]. Another possibility is that activity could evolve over the time course of behavior in freely moving animals such that a mixture of inputs from local circuitry and long-range circuits could function like attractor networks to shape output into one of a few convergent states (**Figure 8B**), consistent with attractor networks in the hypothalamus[71]. A third possibility is that valence may emerge in combination with behavior and internal state. In this model, the plCoA integrates sensory information with other state variables to shift the activity towards one output. If either of these latter two models is correct, recording activity over longer time scales in freely moving animals could provide insight into how activity correlates with behavior. Alternatively, valence signals may arise downstream of plCoA, but molecular mechanisms to support this model are currently undescribed, and such a model would be at odds with our finding of divergent valence-specific circuitry required attraction and aversion. Moreover, innate behavior is dynamic and more complex than simple attraction and avoidance and it is possible that the neural activity is as dynamic, changing over the course of behavior. Thus, it will be important to investigate activity of in the plCoA in behaving animals.

A unique amygdala circuit motif for valence using a population code

The widespread circuit model for valence encoding centers on divergence, in which information is routed to different pathways depending on the valence of the stimulus. The plCoA circuit we have identified is anatomically similar, but unique in its encoding properties. Most divergent circuits function to generalize stimuli, discarding information about stimulus identity to simplify to low dimensional valence signals from distinct neuronal populations. In contrast, the plCoA groups stimuli, using a high dimensional code of odor identity that appears to be routed through divergent projections to mediate opposing responses. In this model, the valence of an odor could be determined based on the population dynamics and composition within a distributed, sparse population code that ultimately funnels information through divergent pathways corresponding to their innate significance. Such a model could serve to increase the flexibility of the system while retaining the ability to yield stereotyped responses.

Limitations of the study

The odorant, TMT, is a thiol containing odorant and has long been suspected of acting as an irritant through the trigeminal system and it is known to activate TrpA1 channels in trigeminal neurons[72]. However, other work has shown that removal of the olfactory bulb or $ZnSO_4$ disruption of OSNs eliminates TMT evoked freezing, whereas lesion of the trigeminal nerve does not[73, 74]. Further, in our assay, TMT avoidance requires the olfactory bulb, and plCoA circuitry indicating the involvement of the olfactory system in TMT evoked behaviors[14]. Thus, despite the differences in observations in underlying pathways for TMT responses, the aversion measured in our assay is dependent on olfactory pathways but there is a potential for it to also engage the trigeminal pathway.

775 The conclusion that the plCoA circuitry mediates approach and avoidance is limited by
776 the use of only one attractive and one aversive odor in our behavioral experiments. Thus, it
777 remains unclear how these findings generalize to other odors. The fact that exogenous
778 activation of different pathways is sufficient to producing behaviors of opposite valence suggests
779 that there are dedicated plCoA outputs for different behaviors, but the broader necessity
780 remains to be tested. Moreover, it remains unclear how odor activates neurons with distinct
781 projections. Although we did not observe generalized valence responses to odor in calcium
782 imaging experiments, our investigation only concerns the activity of general plCoA ensembles,
783 not of specific neurons. Thus, it remains possible that neurons projecting to the NAc or MeA are
784 more likely to respond to attractive or aversive odors, respectively. However, we did not observe
785 any bias in odor response based on topographical location, and projection defined neurons are
786 topographically distributed.

787 We provide evidence that plCoA projections to the NAc and MeA are necessary and
788 sufficient for attraction and avoidance. However, it remains unclear what the projections from
789 the plCoA to other areas contribute to odor evoked behavior. For instance, the BNST and LS
790 have been implicated in arousal and sustained anxiety, respectively. Thus, it is possible that
791 those projections mediate aspects of behavior beyond attraction and avoidance that were not
792 assessed in our assay.

793

FIGURE LEGENDS

Figure 1. The plCoA encodes innately-valenced odor identity using a population code.
(A) Schematic representation of virus injection and GRIN lens implantation into aplCoA or pplCoA for two-photon microscopy.
(B-C) Representative images (**B**) and traces (**C**) of fluorescence changes in individual neurons over an approximately 20-minute period that includes periods of odor stimulation.
(D) Schematic of odor exposure paradigm. Each trial presented 5 seconds of odor followed by a variable inter-trial interval (20-30s). Odors were present in blocks of 20 trials per odor, with 2 counterbalanced block schedules (1 & 2). Six odors were used: the appetitive odors 2-phenylethanol (2PE) and peanut oil (PEA), the neutral odors heptanol (HEP) and isoamyl acetate (IAA), and the aversive odors trimethylthiazoline (TMT) and 4-methylthiazoline (4MT).
(E) Heatmap of trial-averaged and Z-scored odor-evoked activity over time from pooled plCoA neurons. Responses are grouped by hierarchical clustering, with the dendrogram (right). Odor delivery marked by vertical red lines.
(F) Average of trial-averaged and Z-scored odor-evoked activity for each cluster concatenated. The order of color-coded blocks corresponds to the order of clusters in (**E**).
(G) Proportion of neurons responsive to different numbers of odors. Bars represent the mean across 13 animals and the error bars show SEM.
(H) Proportion responsive to each odor for aplCoA (red) or pplCoA (blue).
(I) Valence scores of individual neurons. White circles show the median of each distribution, whereas the gray rectangle shows the 25th-75th percentile range.
(J) Proportion of neurons with significant valence scores calculated as a function of trial number. Calculated with a 10-trial moving window. Top half shows those with significant positive valence scores, the bottom half shows those with significant negative valence scores.
(K) The percentage of neurons with responses (Z>2 for at least 5 frames) as a function of trial number for each odor.
(**L**) Left, MNR accuracies for all pooled plCoA neurons (data) and a control distribution where the training labels are shuffled (shuffled) in a violin plot. Right, proportion of neurons in each animal that have MNR accuracy greater than the 95th percentile of the shuffled MNRs.
(**M**) Cross-validated average accuracies of multinomial SVM's plotted as a function of the number of neurons used for training during the odor period. Circles represent the mean across 100 iterations of random sampling of neurons and error bars show the standard deviation.
(**N**) Cross-validated accuracy of ecoc-SVM classifiers for a 6-odor classification task trained using 200 neurons as a function of time. Lines indicate means and shaded areas show the standard deviation across 100 random samplings of 200 neurons from the pooled data, and shuffled training controls where the label vectors are randomly shuffled.
(O) An example confusion matrix for a multinomial SVM trained with 200 neurons.
(Q) Comparison of inter-valence and intra-valence confusion across number of neurons used in training the classifiers. Filled circles show the average of the data across 100 iterations, open circles show shuffled controls.
(4) The normalized average distance between odor pairs that have different valence (inter) or same valence (intra).

836 Across panels, ns, not significant. Additional specific details of statistical tests can be found in
837 Supplemental Table 1.

838 **Fig. 2. The plCoA has topographic organization capable of driving approach and**
839 **avoidance behaviors.**
840 **(A)** Schematic of plCoA domains divided into anterior (aplCoA), middle (mplCoA), and posterior
841 (pplCoA) regions based on histology, positioning, and gradients observed in past
842 observations[23].
843 **(B)** Strategy to activate anterior-posterior topographical ensembles via optogenetics.
844 (**C**) Representative histology and fiber/virus placement for aplCoA and pplCoA ChR2 animals.
845 (**D**) Schematic of four-quadrant open field behavioral assay with closed-loop photostimulation.
846 **(E-F)** Linear-fit of change in performance index (**E**) or mean port distance (**F**) as a function of
847 anterior-posterior position along plCoA for optical stimulation.
848 **(G)** Paths traveled during the stimulus period for a representative mouse (left) and baseline-
849 normalized collective heatmaps (right) from both the ChR2- and eYFP-infected groups with
850 aplCoA-localized fiber implants. Lower right stimulus quadrant indicated in blue.
851 **(H-I)** Mean effect of Photostimulation of aplCoA neurons on time spent in stimulated quadrant
852 (performance index) (**K**) and distance from the corner (port distance) (**I**).
853 **(J)** Paths traveled during the treatment period for a representative mouse (left) and baseline-
854 normalized collective heatmaps (right) from both the ChR2- and eYFP-infected groups with
855 pplCoA-localized fiber implants. Lower right stimulus quadrant marked in blue.
856 (**K-L**) Mean effect of photostimulation of pplCoA neurons infected with ChR2, but not eYFP, is
857 sufficient to increase time spent in the stimulation quadrant (**K**) and reduce its average distance
858 from the stimulation port during the stimulation period (**L**).
859 Abbreviations: aplCoA, anterior zone of posterolateral cortical amygdala; mplCoA, middle zone
860 of posterolateral cortical amygdala; pplCoA, posterior zone of posterolateral cortical amygdala.
861 Across panels, ns, not significant; * $p < 0.05$; ** $p < 0.01$; *** $p < 0.001$. Specific details of
862 statistical tests can be found in Supplemental Table 1.

863 **Fig. 3. Transcriptomic heterogeneity of plCoA molecular cell types.**
864 **(A)** Schematic of freeze and-re-pool strategy for snRNA-seq.
865 **(B)** Two-dimensional UMAP (n = 47,132 nuclei, see also **Figure S4.3**), colored by broad cellular
866 identity assigned by graph-based clustering of neuronal and non-neuronal nuclei.
867 (**C**) Cell-type-specific expression of canonical marker genes indicating broad cellular identity in
868 the brain. Dot size is proportional to percentage of nuclei expressing the marker, with color
869 scale representing normalized expression level.
870 (**D**) Total proportion of cells of each identified type in each domain of plCoA.
871 **(E)** Two-dimensional UMAP of glutamatergic neurons, colored by molecular cell type.
872 **(F)** Clustered heatmap showing Euclidean distance between averages of each subtype
873 positioned based on hierarchical clustering (left), and dot plot of marker genes for all
874 glutamatergic subtypes (right).
875 **(G)** Two-dimensional UMAP of GABAergic neurons, colored by molecular cell type, like in (**E**).
876 **(H)** Clustered heatmap showing Euclidean distance between averages of each subtype
877 positioned based on hierarchical clustering (left), and dot plot of marker genes for all GABAergic
878 subtypes (right), like in (**F**).

879

880 **Fig. 4. Glutamatergic neurons subtypes in plCoA are spatially distributed along an**
881 **anteroposterior molecular gradient.**
882 (**A**) UMAP of all plCoA nuclei colored by zone of origin, with dotted outlines and labels denoting
883 the major cell types.
884 (**B**) Relative proportion of nuclei from each domain within each broad identity class. Dotted line
885 indicates chance level for all plCoA nuclei.
886 (**C**) Top, abundance of domain-specific DEGs for each major cell type, either enriched in
887 aplCoA nuclei (top) or pplCoA nuclei (bottom). Bottom, volcano plots for domain-specific DEGs
888 for glutamatergic (left) and GABAergic neurons (right), the two cell types with the greatest
889 degree of domain specific gene expression, where negative log-fold changes indicate
890 enrichment in pplCoA and positive log-fold changes indicate enrichment in aplCoA.
891 (**D**) UMAP of plCoA glutamatergic neurons colored by domain of origin, with dotted outlines and
892 labels denoting the subtypes on the graph. Groups of glutamatergic neuron types identified
893 previously via Euclidean distance and hierarchical clustering are overlaid on top of the neuron
894 types of interest.
895 (**E**) Relative proportion of molecular subtypes from each domain within glutamatergic neurons,
896 where relevant subtypes are outlined according to their glutamatergic neuron group. Dotted line
897 indicates chance level for plCoA glutamatergic neuron nuclei.
898 (**F**) UMAP of all glutamatergic neuron nuclei, colored by expression levels of *VGluT2* (top) or
899 *VGluT1* (bottom).
900 (**G**) Left, representative images of *in situ* RNAscope labeling of *VGluT2* RNA (red) and *VGluT1*
901 RNA (green) across plCoA domains. Right, proportions of glutamatergic neurons expressing
902 *VGluT2, VGluT1,* or both. Scale bars, 500 μm (main image), 50 μm (inset).
903 (**H**) UMAP of all plCoA-overlapping Visium capture spots, colored by cluster. Broad spatial
904 position of groups of clusters are overlaid on top of the capture spots of interest.
905 (**I**) UMAP of all plCoA-overlapping Visium capture spots, colored by expression levels of *VGluT2*
906 (top) or *VGluT1* (bottom).
907 (**J**) Representative plCoA-overlapping region of one section on a Visium slide capture area, with
908 capture spots colored by cluster.
909 (**K**) Representative plCoA-overlapping region of one section on a Visium slide capture area, with
910 capture spots colored by expression levels of *VGluT2* (top) or *VGluT1* (bottom).
911 (**L**) Prediction scores for representative glutamatergic neuron subtypes within Group 1 (left) and
912 Group 2 (right), shown on a UMAP of all plCoA-overlapping capture spots across all sections
913 (top) and on a representative plCoA-overlapping region of one section (bottom).
914 (**M**) Prediction scores for a representative GABAergic neuron subtype, shown on a UMAP of all
915 plCoA-overlapping capture spots across all sections (top) and on a representative plCoA-
916 overlapping region of one section (bottom).
917 Across panels: * $p < 0.05$; ** $p < 0.01$; *** $p < 0.001$; ns, not significant. Additional specific
918 details of statistical tests can be found in Supplemental Table 1.

919

920

921 **Fig. 5. Glutamatergic plCoA$^{VGluT2+}$ and plCoA$^{VGluT1+}$ neurons contribute to innate approach**
922 **and avoidance behaviors.**
923 (**A**) Schematic for selective photostimulation of distinct glutamatergic cell type. *VGluT2::Cre* and
924 *VGluT1::Cre* animals were injected with Cre-dependent viral vectors into mplCoA with a fiber
925 optic implant placed just above the injection site.
926 (**B**) Representative histology from ChR2 viral injection and fiber implantation site in an
927 *VGluT2::Cre* animal (top) and an *VGluT1::Cre* animal (bottom).
928 (**C**) Baseline-normalized collective heatmaps from both the ChR2- and eYFP-infected groups in
929 *VGluT2::Cre* and *VGluT1::Cre* animals with plCoA-localized fiber implants. Lower right stimulus
930 quadrant marked in blue.
931 **(D-G)** Effect of photostimulation of plCoA$^{VGluT2+}$ neurons (**D-E**) or plCoA$^{VGluT1+}$ neurons (**F-G**) on
932 time spent in the stimulation quadrant (**D, F**) and distance from the corner (**E, G**).
933 (**H**) Behavioral paradigm to assess innate valence responses to odor. Left, schematic of four-
934 quadrant open field behavioral assay for spatially-specific odor delivery. Upper right, within-trial
935 timeline. Lower right, odors delivered and their associated innate valence.[3]
936 (**I**) Schematic of strategy for selective chemoinhibition of molecularly defined glutamatergic
937 plCoA neurons.
938 (**J-M**) Effect of chemoinhibition of plCoA $^{VGluT1+}$ neurons on time spent in the odor quadrant (**J, L)**
939 or decrease in mean port distance (**K, M**) in response to 2PE (**J-K**) or TMT (**L-M**).
940 (**N-Q**) Effect of chemoinhibition of plCoA $^{VGluT2+}$ neurons on time spent in the odor quadrant (**N,**
941 **P)** or decrease in mean port distance (**O, Q**) in response to 2PE (**N-O**) or TMT (**P-Q**).
942 Across panels, ns, not significant; * $p < 0.05$; ** $p < 0.01$; *** $p < 0.001$, **** $p < 0.0001$.
943 Additional specific details of statistical tests can be found in Supplemental Table 1.

944 **Fig. 6. Projections to MeA and NAc from plCoA are Topographically Organized**
945 (**A**) Left, whole-hemisphere view at AP = 0.98 mm from bregma. Scale bar, 500 μm. Right,
946 Magnified images of the areas highlighted inside white dashed lines. Scale bar, 200 μm.
947 (**B**) Left, whole-hemisphere view at AP = -1.06 mm from bregma. Scale bar, 500 μm. Right,
948 Magnified images of the areas highlighted inside white dashed lines. Scale bar, 200 μm.
949 (**C**) Other plCoA projections not found in cross-sections of the brain found in **(A)** and **(B)**. Scale
950 bar, 200 μm.
951 (**D**) Magnitude of anterograde synaptophysin-eYFP fluorescence in primary downstream targets
952 of plCoA projection neurons ordered by total output strength, colored based on each region's
953 function.
954 (**E**) Schematic for topographic retrograde mapping strategy from MeA and NAc into plCoA. Red
955 retrobeads are injected into MeA or NAc and topographical projection bias is examined along
956 the anterior-posterior axis.
957 (**F**) Representative images (top) for injection into MeA (left) or NAc (right) and number of
958 neurons labeled along the anterior-posterior axis as distance (mm) from bregma (bottom). Gray
959 lines denote individual replicates, where colored lines indicate mean ± s.e.m.
960 (**G**) Proportion of retrobead-labeled neurons projecting to MeA or NAc for each 100 μm segment
961 as a function of distance from bregma. Dashed line indicates overall balance of all retrobead-
962 labeled neurons across entire plCoA.

(**H**) Proportion of retrobead-labeled neurons from either target within each plCoA zone. MeA-labeled neurons are significantly enriched in aplCoA compared to NAc-labeled neurons, while NAc-labeled neurons are significantly enriched in pplCoA compared to those labeled from MeA.
(**I**) Representative histological images for the injection sites in aplCoA (left) and pplCoA (right) from a representative animal. Scale bar, 200 µm.
(**J**) Representative histological images for MeA from the animal in (**J**). Scale bar, 200 µm.
(**K**)**.** Representative histological images for NAc from the animal in (**J**). Scale bar, 200 µm.
(**L**) Output strength as a proportion of total fluorescence from aplCoA and pplCoA to MeA and NAc.
(**M**) Representative histological images for the injection site in plCoA from a representative *VGluT1::Cre* and *VGluT2::Cre* animal. Scale bar, 200 µm.
(**N**) Representative histological images from MeA and NAc from a representative animal of either genotype. Scale bar, 200 µm.
(**O**) Left, output strength as a proportion of total fluorescence from plCoA$^{VGluT2+}$ and plCoA$^{VGluT1+}$ neurons to MeA and NAc. Right, comparison of same data, but by target region within genotype.
(**P**) Same data as **(O)**, but by target region within genotype.
(**Q-V**) Mapping collateral projections from NAc- and MeA projecting neurons.
(**Q**) Representative histological images for the injection site in plCoA from a representative animal receiving retrograde virus into MeA or NAc. Scale bar, 200 µm.
(**R**) Representative histological images of NAc and MeA retro-Cre targeting (red) and outputs (green).
(**S**) Comparison of absolute integrated fluorescence intensities in MeA and NAc when retroAAV was injected into NAc (top) or MeA (bottom).
(**T**) Quantification of fluorescence in selected downstream brain regions from plCoA originating from plCoA-NAc neurons proportional to eYFP fluorescence in NAc (top) or MeA (bottom).
Abbreviations: NAc, nucleus accumbens; BNST, bed nucleus of stria terminalis; MeA, medial amygdala; Pir, piriform cortex; BLA, basolateral amygdala; Ahi, amygdalo-hippocampal transition area; pmCoA, posteromedial cortical amygdala; Str, striatum; OT, olfactory tubercle; EA, extended amygdala; IPAC, inferior peduncle of the anterior commissure; AA, anterior amygdala; LA, lateral amygdala; HDB, horizontal limb of the diagonal band; VP, ventral pallidum; AIC, anterior insular cortex; mfb, medial forebrain bundle; MO, medial orbitofrontal cortex; LOT, lateral olfactory tract; ACo, anterior cortical amygdala; AOA, anterior olfactory area; DG, dentate gyrus; Rt, reticular nucleus; LPO, lateral preoptic area; VMH, ventromedial hypothalamus; DEn, dorsal endopiriform claustrum; LH, lateral hypothalamus; IL, infralimbic cortex; DP, dorsal peduncular cortex; LS, lateral septum; CxA, cortex-amygdala transition area; sox, supraoptic decussation; StHy, striohypothalamic nucleus; GP, globus pallidus; PLH, perirhinal cortex; ZI, zona incerta.
Across panels, ns, not significant; * $p < 0.05$; ** $p < 0.01$; **** $p < 0.0001$. Additional specific details of statistical tests can be found in Supplemental Table 1.

1004 **Fig. 7. Projections from plCoA to NAc and MeA control innate olfactory attraction and**
1005 **aversion.**
1006 (**A**) Schematic for optogenetic MeA terminal stimulation in plCoA neurons. Strategy to activate
1007 MeA-projecting plCoA neuron terminals via optogenetics (top) and representative histology from
1008 ChR2 viral injection and fiber implantation site (bottom).
1009 (**B**) Baseline-normalized collective heatmaps from both the ChR2- and eYFP-infected plCoA
1010 groups with MeA- and NAc-localized fiber implants. Lower right stimulus quadrant marked in
1011 blue.
1012 **(C-D)** Optogenetic MeA terminal stimulation of plCoA neurons infected with ChR2, but not
1013 eYFP, is sufficient to reduce time spent in the stimulation quadrant (**C**) and increase its average
1014 distance from the port (**D**) during the stimulation period.
1015 **(E-F)** Optogenetic NAc terminal stimulation of plCoA neurons infected with ChR2, but not eYFP
1016 is sufficient to increase time spent in the stimulation quadrant (**E**) and decrease its average
1017 distance from the stimulation port (**F**) during the stimulation period.
1018 (**G**) Viral strategy for selective retrograde chemoinhibition of projection-defined plCoA neurons.
1019 (**H**) Schematic for selective retrograde chemoinhibition of projection-defined plCoA neurons.
1020 (**I-L**) Chemoinhibition of NAc-projecting plCoA neurons significantly eliminates the 2PE-evoked
1021 increase in time spent in the odor quadrant (**I)** and decreases in mean port distance (**J).** The
1022 response to TMT is unaffected in time spent in odor quadrant (**K**) or port distance (**L**).
1023 (**M-P**) Chemoinhibition of MeA-projecting plCoA neurons does not affect 2PE-evoked increase
1024 in time spent in the odor quadrant (**M)** or decrease in mean port distance (**N)** significantly
1025 decreases the TMT-evoked reduction in time spent in the odor quadrant (**O)** or increase in mean
1026 port distance (**P).**
1027 Across panels, ns, not significant; * $p < 0.05$; ** $p < 0.01$; *** $p < 0.001$. Additional specific
1028 details of statistical tests can be found in Supplemental Table 1.

1029

1030 **Figure 8. Models that could support innate odor evoked attraction and avoidance.**
1031 Two potential models that could support valence responses to odor with a population code
1032 imposed on divergent circuitry.
1033 (**A**) Balance of activation between MeA- and NAc-projecting neurons determines the valence. In
1034 this model an odor may activate a different proportion of these projection defined neurons, and
1035 the valence is determined by the balance. For example activation of more NAc-projecting
1036 neurons should cause attraction, and activation of more MeA-projecting neurons should cause
1037 aversion.
1038 (**B**) Dynamic activity evolves overtime due to recurrent processing or integration of behavioral
1039 state variables, in an attractor-like network. In this case the activity may evolve from an initional
1040 broad population code (T_0) towards preferential activation of one output population over time
1041 (T_n).

ACKNOWLEDGMENTS

We thank the entire Root lab for helpful discussion and support. We thank B. Lim for provision of the AAVDJ-hSyn-Flex-mRuby-T2A-SynEGFP virus. We thank G. Pekkurnaz, N. Spitzer, and M. Pratelli for reagents and facilities support. We also thank C. O'Connor and L. Boggeman at the Salk flow cytometry core, and N. Hah at the Salk next-generation sequencing core. We thank D. Jimenez for assistance with histology and colony management. This publication includes data generated at the UC San Diego IGM Genomics Center utilizing an Illumina NovaSeq 6000 that was purchased with funding from a National Institutes of Health SIG grant (#S10 OD026929). This work was generously supported by the National Defense Science and Engineering Fellowship (J.R.H.), CIHR Postdoctoral Fellowship (F.M.), JPB Foundation, the PIIF, PNDRF, JFDP, New York Stem Cell Foundation, Klingenstein Foundation, McKnight Foundation, Salk Institute, Howard Hughes Medical Institute, Clayton Foundation, Kavli Foundation, Dolby Family Fund (K.M.T.), the Hellman Fellowship (C.M.R.), and the National Institutions of Health, via grants through the NIA (RF1AG061831-01S1, P.A.D.), NIMH (K99MH121563-02, F.M.; R01MH115920-03 and R37MH102441, K.M.T.), NIDDK (DP2DK102256-01S1, K.M.T.), and NCCIH (DP1AT009925-04, K.M.T.), and the NIDCD (R00DC014516-05 and R01DC018313-01A1, C.M.R.).

AUTHOR CONTRIBUTIONS

J.R.H. and C.M.R. conceived the project. J.R.H., C.L.C., D.L., M.B., J.H.L. and A.N.Z. performed surgeries and analyzed histological data. J.R.H., C.L.C., and A.N.Z. performed behavioral experiments, managed the colony, and analyzed behavioral data. J.R.H. and D.L. performed calcium imaging experiments and analyzed calcium imaging data. J.R.H. performed sequencing experiments, analyzed sequencing data, and prepared all figures. H.K.R. and P.A.D. designed and performed spatial transcriptomics experiments and provided data for analysis. F.M., M.E.L., and K.M.T. provided the CellProfiler processing pipeline, as well as intellectual, facilities, and logistic support and guidance. C.M.R. supervised the project. J.R.H., D.L., M.B., H.K.R., and C.M.R. wrote the manuscript. All authors edited the manuscript.

DECLARATION OF INTERESTS

The authors declare no competing interests.

RESOURCE AVAILABILITY

Lead contact

Further information and requests for resources and reagents should be directed to and will be fulfilled by the Lead Contact, Cory M. Root (cmroot@ucsd.edu).

Materials availability

This study did not generate new unique reagents.

Data and code availability

All snRNA-seq and Visium spatial sequencing data generated for this study is deposited on Gene Expression Omnibus (GEO): GSE270798. All other data reported in this paper will be shared by the lead contact upon request. The code used to analyze all data and generate all graphs can be found online at Zenodo: Any additional information required to reanalyze the data reported in this paper is available from the lead contact upon request.

EXPERIMENTAL MODEL AND SUBJECT DETAILS

All procedures at the University of California, San Diego, and Columbia University were performed in accordance with Institutional Animal Care and Use Committee protocols in accordance with NIH guidelines. All mice were provided food and water ad libitum and maintained on a regular 12-hour reverse light/dark cycle at room temperature, with weight, health, and immune status monitored daily and verified to be within normal ranges. Mouse cages were changed regularly based on degree of soiling. All mice were group-housed with randomly assigned littermates prior to surgery, and single-housed after surgery. All animals were used in a single experiment each, except for a subset of mice who underwent 4-quad, EPM, and OFT experiments, who performed each test in no specific order.

Subject Details for Sequencing Experiments

Subject details for single-nucleus sequencing

All mice for snRNA-seq in the study were males on the wild-type C57BL/6J background (RRID:IMSR_JAX:000664) and received directly from Jackson Laboratories at 6 weeks of age and acclimated to the colony prior to experiments. Animals were single-housed and placed into sensory deprivation 24 hours prior to sacrifice to reduce artifactual immediate early gene expression. Sacrifice was performed at P60 ± 3 days (n = 5-10 mice per pool). Sample size was determined based on number of expected nuclei per region per mouse: estimates of expected nuclei were determined empirically, though nuclear recovery was approximately 20% of total based on cellular density estimates from the Blue Brain Cell Atlas. 20,000 nuclei were targeted per combination of assay, condition, and region, which was determined using SCOPIT v1.1.4, allowing potential detection of at least 10 nuclei from 10 rare subpopulations at 0.1% frequency with 95% probability[75]. A total of 50 mice were used for this purpose.

Subject details for spatial transcriptomics

In the separate study for spatial transcriptomics, APP23 (B6.Cg-Tg(Thy1-APP)3Somm/J; C57BL/6J background, RRID:IMSR_JAX:030504) non-transgenic (NTG) littermates control mice were housed in light-tight enclosures[76]. The mice were given ad libitum food and water access. This study used a total of 17 mice almost equally distributed across sex, of which sections from 11 sagitally bisected the plCoA and were used in downstream analysis. No analysis of sex differences was performed due to inaccessibility of that information on a per-

section basis. However, no such differences were apparent from per-section gene expression correlations reported in supplementary information.

Subject Details for Calcium Imaging, Tracing, and Activity Manipulations

Subject details for wild-type experiments

All mice for topographic and projection-defined manipulation and tracing experiments, as well as calcium imaging, were males on the wild-type C57BL/6J background and received directly from Jackson laboratories before 12 weeks of age. After surgery, mice incubated for at least 21 days if injected with virus or at least 7 days if injected with a retrograde tracer (e.g. retrobeads, cholera toxin B) to allow virus to express and tracers to travel in retrograde, respectively. All surgeries and downstream experiments were performed on mice at least 8 weeks of age.

Subject details for transgenic experiments

We used VGlut2-IRES-Cre (Slc17a6tm2(cre)Lowl; C57BL/6J background, RRID:IMSR_JAX:028863; *Slc17a6::Cre*) and VGlut1-IRES2-Cre-D (Slc17a7tm1.1(cre)Hze; C57BL/6J background, RRID:IMSR_JAX:023527; *Slc17a7::Cre*) strain mice for molecularly defined optogenetic stimulation experiments and genotype-specific tracing. These mice were bred on-site at UCSD and were genotyped in-house using genomic DNA from ear tissue amplified with the default primer sets listed by Jackson Laboratories. All mice used for experiments had a heterozygous genotype for the transgenic construct of interest. After surgery, mice incubated for at least 21 days to allow viral expression.

METHODS DETAILS

Stereotactic surgery procedures

All surgeries were performed under aseptic conditions using a model 1900 digital small animal stereotaxic instrument (Kopf Instruments). Mice were initially anesthetized in a sealed box containing 5% gaseous isoflurane, and then deeply anesthetized using isoflurane (2.5% in 1L/min of O_2) during surgeries (VetFlo, Kent Scientific Corporation). We immobilized and leveled the head in a stereotaxic apparatus (Kopf Instruments), removed fur from the scalp by shaving, applied eye lubricant (Optixcare), cleaned the incision site with 70% ethanol and betadine prior to incision, peeled off connective tissue, and dried the surface of the skull prior to craniotomy before proceeding with injections and implantations specific to certain experiments. All virus injections were performed at 2 nL/sec using a pulled glass pipette (Drummond) and a Nanoject III pressure injector (Drummond). To prevent backflow, the pipette was left in the brain for 15 minutes after injection.

Surgeries for calcium imaging

Surgeries for imaging experiments were performed in a manner similar to that previously described[20]. The skull was prepared with OptiBond™ XTR primer and adhesive (KaVo Kerr)

prior to the craniotomy. After performing a craniotomy 1 mm in diameter centered around the virus injection site, a 27G blunt needle was used to aspirate ~2.5 mm below the brain surface. 600 nl of AAV9-hSyn-FLEX-jGCaMP8s-WPRE (2.5 × 10^{13} gc/ml, Addgene) was diluted to ~1 × 10^{12} gc/ml gc/ml and injected into the left middle plCoA in two 300 ul boli, one in layer 2 and one 400 um dorsal (+0.4 DV) in layer 3. Following the viral injection, a head-plate (Model 4, Neurotar) was secured to the mouse's skull using light-curing glue (Tetric Evoflow, Ivoclar Group). At least 30 minutes after viral injection, a 1 mm GRIN lens (NA, ~1.9 pitch, GrinTech) was sterilized with Peridox-RTU then slowly lowered at a rate of 500 um/min into the craniotomy until it was 200 um dorsal (+0.2 DV) to the injection coordinate. The lens was adhered to the surface of the skull using Tetric Evoflow. We then placed a hollow threaded post (AE825ES, Thorlabs) to act as a housing for the lens and adhered it using Tetric Evoflow. Any part of the skull that was still visible was covered using dental cement (Lang Dental). Finally, the housing was covered with a Nylon cap nut (94922A325, McMaster-Carr) screwed onto the thread post to protect the lens in between imaging. Animals were left on the heating pad until they fully recovered from anesthesia.

Surgeries for optogenetic stimulation

For optogenetic topographic- or projection-specific stimulation experiments, we injected wild-type C57BL/6J mice between 2-4 months of age with 100 (if topographic) or 150 (if projection-specific) nL of either AAV5-hSyn-eYFP (3.3 × 10^{12} gc/ml, UNC Vector Core) or AAV5-hSyn-ChR2-mCherry-WPRE-PA (4.1 × 10^{12} gc/ml, UNC Vector Core). For Cre-dependent molecularly defined optogenetic stimulation, we injected 200 nl AAV5-EF1A-DIO-hChR2(H134R)-eYFP (5.5 × 10^{12} gc/ml, UNC Vector Core) or AAV5-EF1A-DIO-eYFP (4.0 × 10^{12} gc/ml, UNC Vector Core) All such injections were left unilateral, into either aplCoA or pplCoA for topographic photostimulation, and into middle plCoA for projection- or genotype-specific photostimulation. For topographic and genotype-specific photostimulation animals, we implanted the fiber 300 um (+0.3 DV) directly above the injection site with all other coordinates remaining constant. Anterior-posterior axis positioning arose from stochastic variation in virus and fiber placement. For projection-specific photostimulation animals, we implanted the fiber 300 um (+0.3 DV) directly above either the MeA or NAc, holding all other coordinates for the two regions constant as described above. For all optogenetic stimulation experiments, we implanted a fiber optic cannula (2.5 mm ferrule outer diameter, 200 um core, 0.39 numerical aperture; RWD) 300 um above the targeted stimulation site. These fibers were affixed onto the skull using OptiBond XTR (Kerr) and stably secured with Tetric Evoflow (Ivoclar Vivadent) coated with cyanoacrylate (Toagosei). After surgery, we injected all mice with 0.04 mL Buprenorphine SR (Ethiqa XR, Fidelis) for pain management. All mice were singly housed immediately after surgery and returned to the colony once ambulatory.

Surgeries for chemogenetic inhibition

For all plCoA inhibition experiments, we bilaterally injected C57BL/6J mice between 2-4 months of age with 250 nL of either AAV2-hSyn-DIO-hM4D(Gi)-mCherry (7.1 × 10^{12} gc/ml, Addgene) or AAV2-hSyn-mCherry (1.8 × 10^{13} gc/ml, Addgene) virus. For projection-specific inhibition experiments, wild-type C57BL6/J mice were used, and AAVretro-hSyn-EBFP-Cre (1.5 × 10^{12}

gc/ml, Addgene) either 50 nL were injected into MeA or 300 µL were injected into NAc. For genotype specific inhibition experiments, *VGluT2::Cre* or *VGluT1::Cre* mice were used. All injections were bilateral and targeted to middle plCoA.

Surgeries for fluorescent tracing

For non-topographic anterograde tracing experiments, we bilaterally co-injected of mixed 50 nl AAVDJ-hSyn-FLEX-mRuby-T2A-SynEGFP (4.0 × 10^{12} gc/ml, Addgene, a gift from Byungkook Lim) and AAV5-EF1A-mCherry-IRES-Cre-WPRE (1.9 × 10^{12} gc/ml, UNC Vector Core) into middle plCoA (-1.8 AP, +/-2.9 ML, -5.95 DV).[105,106] For topographic anterograde tracing experiments, we unilaterally injected 20 nl AAV8-hSyn-hChR2(H134R)-mCherry (2.1 × 10^{13} gc/ml, Salk GT3 Viral Vector Core) and AAV8-hSyn-hChR2(H134R)-eYFP (3.2 × 10^{13} gc/ml, Salk GT3 Viral Vector Core) into aplCoA (-1.4 AP, -2.8 ML, -5.95 DV) and pplCoA (-2.1 AP, -3.0 ML, -5.95 DV), counterbalancing region by fluorophore. For retrograde topographic tracing experiments, we unilaterally injected Red Retrobeads IX (Lumafluor) into either MeA (50 nl, -1.2 AP, -2.0 ML, -5.5 DV) or NAc (+1.1 AP, -1.35 ML, -4.5 DV), at volumes of 50 nl or 300 nl, respectively. For anterograde collateralization experiments, AAVretro-EF1A-IRES-Cre (1.3 × 10^{13} gc/ml, Addgene) into either MeA or NAc, and AAVDJ-EF1A-DIO-hChR2(H134R)-eYFP-WPRE-pA (4.03 × 10^{13} gc/ml, Salk GT3 Viral Vector Core) was injected into middle plCoA. For genotype-specific anterograde tracing experiments we injected 50 nl AAVDJ-Ef1a-DIO-ChR2(H134R)-eYFP-WPRE-pA into middle plCoA in VGluT2::Cre or VGluT1::Cre mice.

Calcium Imaging

Odor exposure

Odor exposure for imaging experiments was adapted from methods previously described[20]. Odor was delivered to the mouse using a custom-built olfactometer. Compressed medical air was split into 2 gas-mass flow controllers (Aalborg). One flow controller directed a constant rate of 1.5 L/min to a hollowed out teflon cylinder. The other flow regulator was connected to a 3-way solenoid valve (The Lee Co.). Prior to odor delivery, the 3-way valve directs clean air at 0.5 L/min to the teflon cylinder. During odor delivery, the 3-way valve directs air to an odor manifold, which consists of an array of 2-way solenoid valves (The Lee Co.), each connected to a different odor bottle. The kinetics and consistency of odor delivery were characterized using a miniature Photoionization Detector (mPID) (Aurora Scientific) mounted above the odor port. The odors were detected using different gain settings on the PID control box as follows: 1x for TMT and 4MT, 5x for IAA, 10x for Peanut, 2PE and Heptanol. Depending on the trial type, the appropriate 2-way valve opens, directing 0.5 L/min of air flow through the odor bottle containing a kimwipe blotted with 20 ul of odorant, except for 2PE and peanut oil, in which 500 ul was used.

Prior to imaging, mice were habituated to the head fixation device (Neurotar) and treadmill for at least 3 days for at least 5 minutes per session beginning at least 10 weeks after surgery. The treadmill parts were 3D printed using an LCD printer (EPAX) from publicly available designs. Walking behaviors were measured using a quadrature encoder (Broadcom). A video feed of the

1228 animal's face was also recorded using a camera (Basler) with an 8-50mm zoom lens (Arducam)
1229 at 20 Hz with infrared illumination (Lorex Technology). Animals were exposed to the following
1230 odors for 5 seconds: the appetitive odors 2-phenylethanol (Sigma-Aldrich) and peanut oil
1231 (Spectrum), the neutral odors 1-heptanol (Sigma-Aldrich) and isoamyl acetate (Sigma-Aldrich),
1232 and the aversive odors trimethylthiazoline (BioSRQ) and 4-methylthiazole (Sigma-Aldrich).
1233 Within a single contiguous exposure session, each of the 6 odors were provided 20 times with
1234 12-18 seconds of inter-trial interval. Trials were organized into 6 blocks, each of which consisted
1235 of 20 trials of each of the 6 odors in counterbalanced order without any odors of similar innate
1236 valence adjacent to each other in the trial structure.

1237 ***2-photon microscope data acquisition***

1238 Ca^{2+} imaging data was acquired using an Olympus FV-MPE-RS Multiphoton microscope with
1239 Spectra Physics MaiTai HPDS laser, tuned to 920 nm with 100 fs pulse width at 80 MHz. Each
1240 128 × 128 pixel scan was acquired with a 20x air objective (LCPLN20XIR, Olympus), using a
1241 Galvo-Galvo scanner at 5 Hz. Stimulus delivery and behavioral measurements were controlled
1242 through a custom software written in LabVIEW (National Instruments) and operated through a
1243 DAQ (National Instruments). Each imaging session lasted up to 90 minutes and was
1244 synchronized with the stimulus delivery software through a TTL pulse. Animals were excluded
1245 from analysis if histology showed that either the GRIN lens or the jGCaMP8s virus was
1246 mistargeted or the motion during imaging was too severe for successful motion correction.

1247 **Behavioral Assays**

1248 Mice had been handled for 5 days prior to experiments and acclimated to the room for an hour
1249 prior to testing. All behavioral experiments were performed during the dark period of the
1250 light/dark cycle at least an hour away from the switch between the two photoperiods. Not all
1251 mice were run in all assays, as elevated plus maze and open field tests were added after a
1252 significant proportion of four-quadrant data was collected at targeted sample sizes and mice had
1253 already been sacrificed.

1254 For all optogenetic experiments, optical fibers (200 mm, 0.39 numerical aperture, Thorlabs)
1255 were epoxied to 2.5 mm stainless steel ferrules (Precision Fibre Products), and polished with a
1256 fiber optic polishing kit (Thorlabs) to achieve a minimum of 80% transmission. After surgical
1257 implantation, the ferrules protruding from the mouse's head were coupled to an ADR-800A 100
1258 mW 473 nm laser (LaserCentury) via custom-made patch cables with a single rotary joint (Doric
1259 Lenses) between the mouse and laser. Laser intensity was set to 5-8 mW at the end of the
1260 patch cable. For inhibition experiments, all mice were injected intraperitoneally 60 minutes prior
1261 to the beginning of the behavioral trial with either sterile PBS vehicle or with clozapine-N-oxide
1262 (CNO) dihydrochloride (Hello Bio) dissolved in sterile PBS for a dosage of 2 mg/kg.

1263 ***Four quadrant open field assay***

1264 The four-quadrant open-field task was performed as previously described[23]. In short, all
1265 behavioral assays took place in a four-quadrant open field chamber. Airflow was pumped into

each quadrant via gas-mass flow controllers 150 mL/min (Cole-Parmer). Airflow exited the chamber via a 1-inch outlet in the center of the chamber's floor covered by steel mesh, and the outlet was connected a vacuum line with a gas-mass controller set to 750 mL/min. The chamber was housed in the dark and illuminated from below by infrared lighting. A Basler A601FM camera (Edmund Optics) mounted above the chamber recorded videos of behavioral trials at 4 Hz, and custom software written in Labview (National Instruments) tracked the position of the mouse in real time for each frame. The symmetrical four-quadrant open field chamber was contained in a lightproof structure (0-10 lux) and illuminated by infrared lights, removing any potential spatial cues available to the animals with respect to the room or its surroundings. In optogenetic experiments, an additional 5 cm spacer was added to the chamber flush with the walls to raise their height for more naturalistic behavior, and an acrylic ceiling with a top with a circular opening 30.5 cm in diameter was added to prevent escape while allowing the fiber optic cable to move freely.

In optogenetic experiments, the laser was pulsed with 50 ms bins at 10 Hz, and there was a steep gradient from 1 to 10 Hz along the perimeter of the quadrant, increasing as proximity to the corner of the quadrant decreased. Preliminary experiments in topographical stimulation animals identified no clear behavioral effects from the location of the stimulus quadrant itself (data not shown), and all other downstream stimulation experiments exclusively used the lower right quadrant for stimulation to simplify data analysis. The lasers were controlled by TTL modulation from custom Labview software synchronized to the video capture system.

For inhibition experiments, odor was applied by solenoid valves redirecting airflow through 100 mL glass bottles containing 1 μL of a pure odorant on a small piece of Kimwipes. Odorants used were either the previously-validated innately aversive 2,5-dihydro-2,4,5-trimethylthiazoline (BioSRQ) or the innately appetitive 2-phenylethanol (Sigma-Aldrich) on a small piece of Kimwipe.[3] All odors were presented in the lower-right quadrant, and all trials were spaced out with at least an hour between runs, during which vacuum was applied to the chamber. Odors and injection treatments were given in counterbalanced, independent order within experimental groups.

Open field test

The open field is a square arena illuminated to 100-150 lux by ambient lighting. Mice were habituated to the room for at least an hour prior to testing, but otherwise had no prior experience in the arena prior to exposure. Mice were placed in the center of a square arena (27.3 × 27.3 × 20.3 cm, Med Associates) with four transparent plexiglass walls. Overall locomotion, immobility, and time spent in corners and center regions of arena during each epoch was analyzed for each mouse. Immobility was defined as movement under 0.5 cm/s for a period of at least 1 s, while the center was defined as the middle 13.7 × 13.7 cm square in the center of the arena and the corners as the corner regions that do not overlap with the center square in either direction (25% of arena area for each region). For optogenetic experiments, mice were allowed to move freely throughout the arena for 25 min total, with 5-8 mW 473 nm light stimulation pulsed with 50 ms bins at 20 Hz, alternately delivered during the 5-10 min and 15-20 min epochs (OFF, ON, OFF,

ON, OFF). For chemogenetic experiments, mice were allowed to freely move through the area for 10 min total.

Elevated plus maze

The arms of the elevated plus maze were 30.5 × 5.5 cm. The height of the closed arm walls was 15 cm. The maze was elevated 40 cm from the floor and was placed in the center of the behavior room away from other stimuli. Arms were illuminated to 0-10 lux, with infrared illumination. Mice were placed in the center of maze at the beginning of each trial. For optogenetic experiments, mice were allowed to move freely throughout the maze for 15 min total, with 5-8 mW 473 nm light stimulation pulsed with 50 ms bins at 20 Hz delivered during the 5-10 min epoch (OFF, ON, OFF). For chemogenetic experiments, mice were allowed to freely move through the area for 10 min total.

Histology

Section preparation

All sacrifices were performed during the dark period of the light cycle. Animals were anesthetized prior to sacrifice via combined intraperitoneal injection of 150 mg/kg ketamine (Zetamine, Vet One) and 15 mg/kg xylazine (AnaSed, AMRI Rensselaer). Except for animals used in sequencing studies, animals were subject to transcardial perfusion with 10 mL of sterile phosphate-buffered saline (PBS), followed by 10 mL 4% paraformaldehyde (PFA) solution. The brain was then extracted from the animal and placed into a 4% (PFA) solution in PBS for at least 36 hours until it was sectioned on a VT1000S vibratome (Leica). For tissue extracted for non-RNAscope histology, mice were transcardially perfused with 20 ml phosphate buffered saline (PBS) followed by 20 ml 4% paraformaldehyde (PFA) in PBS. All brains were extracted and post-fixed for at least 24 hours in 4% PFA. For tissue extracted for RNAscope, mice under 6 months of age were decapitated once unconscious and their brains were extracted into a square Peel-A-Way embedding mold (Polysciences) and embedded in OCT (Fisher), and then snap-frozen a dry-ice/isopentane slurry and stored at -80˚C until cryosectioning within a month of sacrifice.

Tissue was mounted in 5% agarose and sectioned sagittally on a vibratome for retrograde experiments, or sectioned coronally without mounting for all other non-RNAscope experiments. These sections were cut at 50 µm and stored in PBS before processing. All connectomic quantitation was performed on samples using epifluorescence without immunolabeling to avoid potential bias due to non-stoichiometric antibody binding, while all others were immunolabeled for visualization of viral targeting accuracy and collection of representative images. Immunolabeling of eYFP and other GFP-derived fluorophores was performed using goat anti-GFP primary antibodies (Abcam) and Alexa Fluor 488-conjugated anti-goat secondary antibodies (Invitrogen), while immunolabeling of mCherry and other DsRed-derived fluorophores used rabbit anti-DsRed primary antibodies (Takara) and Alexa Fluor 588-conjugated anti-rabbit antibodies (Invitrogen), all diluted 1:1000 in PBS-T. All non-RNAscope sections were mounted on Superfrost Plus microscope slides (Fisher) and counterstained with Fluoromount-G containing DAPI (SouthernBiotech). Sections were stored long-term at 4˚C.

1346 ***RNAscope fluorescence* in situ *hybridization***

1347 RNAscope sections were cut at 15 µm on a CM 1950 cryostat (Leica) and mounted on
1348 Superfrost Plus slides and stored at -80˚C until processing via RNAscope within a month of
1349 mounting. RNAscope was performed in an RNA-free environment according to manufacturer
1350 instructions using the Multiplex Fluorescent Reagent Kit v2 (Advanced Cell Diagnostics).
1351 RNAscope was performed using the probes *mm-Slc17a7* in the C2 channel, and *mm-Slc17a6* in
1352 the C3 channel, dyed with Opal 520 and Opal 690 in a counterbalanced manner at 1:15,000
1353 concentration to reduce background fluorescence and allow quantitation of unsaturated, clearly-
1354 distinguishable puncta. Processed RNAscope sections were then mounted with Prolong
1355 Antifade Diamond (ThermoFisher) and stored long-term at 4˚C.

1356 ***Fluorescence image acquisition***

1357 Non-RNAscope Images were acquired at 10X magnification with an VS120 slide scanner
1358 (Olympus), with settings held constant within experiments. Confocal fluorescence images for
1359 RNAscope were acquired on an SP8 (Leica) confocal laser scanning microscope using a
1360 40x/1.30NA oil immersion objective. Serial Z-stack images were acquired using the LASX
1361 software at a thickness of 1 µm per Z stack, with 14-21 planes taken per image. Images were
1362 acquired with identical settings for laser power, detector gain, and amplifier offset for each set of
1363 counterbalanced probe-fluorophore combinations.

1364 **Sequencing Data Acquisition**

1365 ***Tissue extraction and cryopreservation for single-cell sequencing***

1366 Once unconscious, mice animals were transcardially perfused with ice-cold, carbogen-bubbled
1367 (95% O2, 5% CO2), nuclease-free, 0.22 µm sterile-filtered artificial cerebrospinal fluid (ACSF)
1368 with a composition of 93 mM N-methyl-D-glucamine, 2.5 mM KCl, 1.2 mM NaH2PO4, 30 mM
1369 NaHCO3, 20 mM HEPES, 25 mM glucose, 5 mM sodium ascorbate, 2 mM thiourea, 3 mM
1370 sodium pyruvate, 13.2 mM trehalose, 12 mM N-acetyl-cysteine, 0.5 mM CaCl2, 10 mM MgSO4,
1371 and 93 mM HCl, at pH 7.3-7.4[32]. Following transcardial perfusion, brains were immediately
1372 extracted and submerged into ice-cold carbogen-bubbled ACSF, with less than 5 minutes
1373 between the beginning of perfusion and final submersion after extraction. Brains were serially
1374 sectioned in ice-cold, carbogen-bubbled ACSF on a VT1000S vibratome (Leica) with
1375 polytetrafluoroethane-coated razor blades (Ted Pella) at 0.15 mm/sec and 100 Hz, dividing the
1376 whole cerebrum into 400 µm coronal slices. Target regions were microdissected from these
1377 slices under a stereomicroscope using a sterile blunt-end needle (22 gauge for CeA, ASt, and
1378 tail of striatum, 16 gauge for dorsal striatum). All regions were targeted using Paxinos &
1379 Franklin, 5th Edition, as reference.[36] Extracted tissue samples were recovered in ice-cold,
1380 nuclease-free, 0.22 µm sterile-filtered cryoprotective nuclear storage buffer, composed of 0.32
1381 M sucrose, 5 mM CaCl2, 3 mM magnesium acetate, 10 mM Trizma hydrochloride buffer (pH
1382 8.0), 1 mM dithiothreitol, 0.02 U/µl SUPERase•In RNAse Inhibitor (Invitrogen), and 1X cOmplete
1383 Protease Inhibitor Cocktail with EDTA (Roche). Tissue was then snap frozen using a metal
1384 CoolRack M90 (Biocision) pre-chilled to -80˚C and stored at -80˚C until nuclear isolation.
1385 Following extraction of tissue regions of interest, remaining portions of sections were fixed in 4%

1386 paraformaldehyde and 4′,6-diamidino-2-phenylindole (DAPI) was applied to sections at 1 µg/ml.
1387 After fixation and staining, sections were mounted and imaged on an VS120 slide scanner
1388 (Olympus). From these images, dissection accuracy was assessed for each region, and
1389 individual samples were only selected for downstream nuclear isolation if the extracted tissue
1390 fell entirely within the defined target regions.

1391 Nuclear isolation procedures were adapted from multiple methods described previously[77, 78].
1392 All procedures were performed on ice, and all solutions were ice-cold, nuclease-free, and 0.22
1393 µm sterile-filtered. Cryopreserved tissue pieces were slow thawed by incubation at 4˚C for 1
1394 hour prior to isolation. Tissue pieces were then pooled and resuspended in nuclear isolation
1395 medium composed of 0.25 M sucrose, 25 mM KCl, 5 mM MgCl2, 10 mM Trizma hydrochloride
1396 buffer (pH 7.4), 1 mM dithiothreitol, 0.04 U/µl RNasin Plus RNAse Inhibitor (Promega), 1X
1397 cOmplete Protease Inhibitor Cocktail with EDTA (Roche), and 0.1% Triton-X. The pooled tissue
1398 pieces in nuclear isolation medium were transferred to a 2 mL Dounce tissue grinder. Tissue
1399 was homogenized by 5 strokes from the loose pestle and 15 followed by the tight pestle, and
1400 the resulting homogenate was filtered through a 40 µm Flowmi cell strainer (Bel-Art) into a 1.5
1401 ml Lo-Bind tube (Eppendorf). The homogenate was then centrifuged with a swinging bucket
1402 rotor at 4˚C and 1000 x g for 8 minutes. Nuclei were then washed with nuclear flow buffer
1403 composed of DPBS with 1% bovine serum albumin, 1 mM dithiothreitol, and 0.04 U/µl RNasin
1404 Plus RNAse Inhibitor (Promega) and centrifuged at 4˚C and 500 x g for 5 minutes, which was
1405 subsequently repeated. Nuclei were finally resuspended in nuclear flow buffer containing 3 µm
1406 DRAQ7 (Cell Signaling Technology) and again filtered through a 40 µm Flowmi cell strainer into
1407 a 5 ml round-bottom polystyrene tube. Each isolation took under 45 minutes to perform, from
1408 homogenization to final suspension.

1409 ***Fluorescence-activated nuclei sorting (FANS)***

1410 FANS was carried out on a FACSAria II SORP (BD Biosciences) using a 70 µm nozzle at 52
1411 PSI sheath pressure. For FANS, debris was first excluded by gating on forward and side scatter
1412 pulse area parameters (FSC-A and SSC-A), followed by exclusion of aggregates (FSC-W and
1413 SSC-W), and finally gating for nuclei based on DRAQ7 fluorescence (APC-Cy7). Nuclei were
1414 successively sorted into 1.5 ml LoBind tubes (Eppendorf) under the purity sort mode. The tube
1415 contained 10X RT master mix without RT Buffer C. 16,000 total nuclei were targeted for
1416 downstream processing, and to account for cytometer errors and subsequent loss of nuclei,
1417 21,000 were sorted into the tube. Nuclei were then immediately processed for snRNA-seq.
1418 FANS conditions were optimized for isolation of debris-free nuclei using the LIVE/DEAD
1419 Viability/Cytotoxicity Kit for Mammalian Cells (Molecular Probes), adding to the final suspension
1420 according to manufacturer instructions and examining on a hemocytometer using an EVOS FL
1421 Cell Imaging System (Thermo Fisher) for enrichment of ethidium homodimer-1-positive nuclei
1422 and the absence of Calcein AM-labeled cellular debris.

1423 ***Tissue extraction and sample preparation for spatial transcriptomics***

1424 Mice were euthanized with CO_2 followed by decapitation, either in the dark or in the light. Brain
1425 hemispheres were collected and placed in OCT and then flash frozen in isopentane in liquid

1426 nitrogen. One hemibrain from each mouse was cryosectioned at -18°C sagittally to a thickness
1427 of 10 mm (~2.8 mm from the midline) using a standard Leica CM1860 cryostat and processed
1428 according to the recommended protocols (Tissue optimization: CG000240 Visium 10X
1429 Genomics; Gene expression: CG000239). The tissue was immediately mounted on a Visium
1430 spatially barcoded slide (10X Genomics). The tissue was covered with OCT and kept at -80
1431 degrees C until it was cryosectioned again starting at the same position to a thickness of 10mm
1432 and mounted onto a Superfrost plus microscope slide (Fisherbrand) for staining. Each section
1433 covered approximately 80% of the 5,000 total spots within their fiducial frame. Slides were
1434 stored at -80˚C until use.

1435 **Library Preparation**

1436 ***Library preparation for single nucleus sequencing***

1437 Nuclear suspensions were converted into barcoded snRNA-seq libraries using the Chromium
1438 Next GEM Single Cell 3' v3.1 Reagent Kits v3.1 Single Index (10X Genomics). Library
1439 preparation for both assays was performed in accordance with the manufacturer's instructions.
1440 10,000 nuclei were targeted during each snRNA-seq library preparation run. 10X libraries were
1441 first sequenced at low depth on a NextSeq 550 Sequencing System (Illumina) to estimate
1442 quality and number of nuclei for each library, followed by deep sequencing on a NovaSeq 6000
1443 Sequencing System. All runs were performed using 2 x 100-bp paired-end reads, outputting
1444 data in 28/8/91-bp read format for snRNA-seq runs.

1445 ***Library preparation for Visium spatial transcriptomics***

1446 Tissue was harvested from 7 month old, non-transgenic littermates from a cross to an App23
1447 Alzheimer's model in a C57BL6/J background (Romero et al., in preparation). Visium spatial
1448 gene expression slides and reagents were used according to the manufacturer instructions (10X
1449 Genomics). Each capture area was 6.5mm x 6.5 mm and contained 5,000 barcoded spots that
1450 were 55 µm in diameter (100 µm center to center between spots) provide an average resolution
1451 of about 1 to 10 cells per spot. Optimal permeabilization time was measured at 24 min. Libraries
1452 were prepared according to the Visium protocol (10X Genomics) and sequenced on a
1453 NovaSeq4 (Illumina) at a sequencing depth of 182 million read pairs. Sequencing was
1454 performed with the recommended protocol in a 28/10/10/100-bp read format. H&E
1455 (Hematoxylin, Thermo; Dako bluing buffer, Dako; Eosin Y, Sigma) staining and image
1456 preparation was performed according to the Visium protocol. H&E-stained sections were
1457 imaged using a Nanozoomer slide scanner (Hamamatsu) Spatial gene expression assay was
1458 performed according to the protocol CG000239.

1459 **QUANTIFICATION AND STATISTICAL ANALYSIS**

1460 **Statistical Analysis**

1461 All statistical details can be found in the figure legends. Sample sizes for behavioral studies
1462 were chosen based on past optogenetic studies for each behavior, which had used 6-15
1463 animals per group. Blinding experimenters was not possible for behavioral, imaging, or

sequencing experiments, given familiarity with subjects, but manual quantitation for connectivity experiments was performed blinded to group with random assignment. All statistical tests were performed in R (v4.2.3) unless otherwise specified. All statistical tests were performed with two tails. Group comparisons were made using two-way analysis of variance (ANOVA) followed by Bonferroni post hoc tests, except where otherwise specified. All behavioral experiments were performed by multiple experimenters across multiple cohorts each composed of multiple litters, with littermates distributed across control and treatment groups, with all such cohorts yielding similar results (data not shown), and topography stimulation experiments were performed across multiple facilities and institutions. Numbers of mice used for all non-sequencing experiments are reported within the relevant figures, figure legends, and the text.

Calcium Imaging Data Analysis

Image processing

Data analysis for calcium imaging experiments was adapted from methods previously described[20]. Ca^{2+} imaging data were first motion-corrected using the non-rigid motion correction algorithm NoRMCorre[79]. Afterwards, neural traces were extracted from the motion-corrected data using constrained nonnegative matrix factorization (CNMF)[80]. Spatial components identified by CNMF were inspected by eye to ensure they were not artifacts. A Gaussian Mixture Model (GMM) was used to estimate the baseline fluorescence of each neuron. To account for potential low-frequency drift in the baseline, the GMM was applied along a moving window of 2,500 frames (500 seconds). The fluorescence of each neuron at each time point t was then normalized to the moving baseline to calculate $\Delta F/F = F_t - F_{baseline} / F_{baseline}$. All subsequent analysis was performed using custom code written in MATLAB (R2022b).

Hierarchical clustering of pooled averaged responses

ΔF/F in response to all 6 odors were averaged across trials then Z-scored. The resulting trial-average values from the following time bins were averaged across time: the first second during each odor, the last second during each odor, and the first second after each odor. The resulting 18-element vectors were sorted into 6 clusters after agglomerative hierarchical clustering using Euclidean distance and Ward linkage.

Responsiveness criteria

To determine how many neurons were responsive to a given odor, we compared ΔF/F at each frame during the 2 second odor period against a pooled distribution of ΔF/F values from the 2-seconds prior to odor onset using a Wilcoxon rank sum test. The resulting p-values were evaluated with Holm-Bonferroni correction to ensure that familywise error rate (FWER) was below 0.05. We also counted the number of neurons that were significantly responsive for at least 4 frames during the odor period to report the total percentage of responsive neurons during odor.

Single-neuron 6-odor classifiers

To test how reliably a single neuron's fluorescence could discriminate between the 6 odors, we assessed the performance of multinomial regression (MNR) classifiers trained on a single neuron's responses to 6 odors. For each neuron and odor pair, we averaged the ΔF/F during the last second of the odor exposure for each trial then Z-scored across all trials. The last second was used because classifier performance is highest during the last second of odor exposure and the first second after odor offset. The resulting feature vector, a single dimensional vector of length 120 (6 odors x 20 trials), was used to train the MNR classifiers. The 5-fold cross-validated accuracies are reported and plotted as violin plots. As a control for each neuron, 100 shuffled classifiers were trained on the data with the odor labels randomly assigned.

Pairwise euclidean distance

To quantify the differences among population-level responses to the 6 odors, we quantified the pairwise Euclidean distance between the trajectories of odor responses. First, we subtracted the ΔF/F values during the 2 seconds prior to odor delivery from each frame then averaged these values across trials for each odor. The pairwise Euclidean distance at each frame was computed for each odor pair and normalized to the maximum pairwise distance measured in all odor pairs at any time bin. These calculations were carried out separately for each animal and then averaged across biological replicates to report the mean and the standard error.

Population classifiers

To assess the discriminability of odor responses in high-dimensional space, we measured the accuracy of error-correcting output codes (ecoc) classifiers. At each time point relative to odor delivery, we pooled ΔF/F values from all trials during which either odor was presented. The feature vector is a multidimensional vector of length 120 (6 odors x 20 trials) and varying width k between 1 and 300. These values were then normalized and used to train a multinomial ecoc classifier using a Support Vector Machine (SVM). The accuracy of the classifier was evaluated via 5-fold cross-validation. To compare the classifier accuracies across different numbers of neurons used for training, we randomly selected varying numbers of pooled neurons and used the ΔF/F values during the last second of odor exposure for training.

Behavioral Data Analysis

Behavioral metrics (i.e. performance index, port distance, center distance, open field time, and total distance) for the four-quadrant preference test, open field test, and elevated plus maze were calculated on sets of coordinates created by identifying the centroid of the mouse in real time in video collected from an overhead camera (Basler) at 4 Hz using custom Labview code and outputting the centroid's coordinates for each frame. The mouse was automatically identified by taking a background greyscale image of the behavioral assay's environment at the beginning of each trial and detecting shapes of a minimum size deviating from the background image by a specific threshold. The centroid was then determined by automated generation of a bounding box for the mouse in each frame in real time and recording the coordinate of the centroid of this rectangle.

Four quadrant task data analysis

Mice were tested as previously described[23]. Mice were placed in the chamber for 25 min experiments and tested no more than once per day. The first 10 min served as a baseline test for spatial or temporal bias within the chamber during the trial, and no stimulus of any sort was provided, while the last 15 min were the test of the manipulation. 15 minutes was chosen to balance time courses of odor responses observed in previous experiments, where appetitive odors tend to yield initial responses that decay, while aversive odors tend to yield responses that grow in magnitude over time. To ensure effects did not arise from ceiling or floor effects in the baseline or from a nonstandard baseline internal state, the mouse had to remain within the stimulus quadrant during the baseline test between ~20-30% of the time or else the experiment was terminated, and the mouse was tested again later. The first 2 minutes of data after the stimulus was introduced were excluded from the analysis to reduce variance and account for novelty of the stimulus without affecting the overall valence of the behavioral response, and the last minute of data was excluded to ensure no minor differences in frames captured could affect analysis. For chemogenetic odor response silencing experiments, animals with vehicle odor responses below an absolute value of 0.1 were excluded from experiments to avoid false negatives from attempting to silence a response that was not observed at baseline, which applied to less than a quarter of overall animals tested across experimental conditions. Performance index represents the percent difference from chance occupancy in the manipulation quadrant, calculated as $PI = (P - 25) / 0.25$; where P is the percentage of time the animal spends in the manipulation quadrant. Mean port distance represents the mean distance of each point to the deepest point into the manipulation quadrant observed at baseline.

Open field test data analysis

For elevated plus maze analysis, all chemogenetic inhibition trials used the entirely of the 10 min test length as a single period, while optogenetic stimulation trials used the mean of the three “OFF” periods to compare to the mean of the two “ON” periods. Three metrics of interest were calculated. Center time was calculated as the proportion of time spent in the middle square of the open field comprising 50% of its total area. Corner time was calculated as the proportion of time spent in the corner squares bounded by the walls and the lines bounding the center region. Time immobile was calculated as the proportion of time when the animal moved less than 1 cm/s for at least a one-second period. Location of the open field and bounding regions was kept constant from trial to trial by registering the apparatus to a bounding box with the same top-down dimensions, and every measured centroid outside of the registered region resulting from shadows cast and other artifacts was interpolated between the closest points before and after within the region.

Elevated plus maze data analysis

For elevated plus maze analysis, all chemogenetic inhibition trials used the entirely of the 10 min test length as a single period, while optogenetic stimulation trials used the mean of the two “OFF” periods to compare to the “ON” period. Three metrics of interest were calculated. Time in the open arms was calculated as the proportion of time spent in the open arms compared to the

1580 whole period of interest and did not include time in the center between the two arms. Open arm
1581 entries measures number of episodes where the centroid is observed outside of the bounds of
1582 the closed arms or the center region, without any minimum time or distance out onto the open
1583 arms. Finally, distance was simply calculated as the distance traveled during each period of
1584 interest. Location of open and closed arms was kept constant from trial to trial by registering the
1585 apparatus to a cross-shaped bounding box with the same top-down dimensions, and every
1586 measured centroid outside of the registered region due to factors like the mouse leaning over
1587 the edge of the open arms, among others, was interpolated between the closest points before
1588 and after within the region.

1589 **Analysis of Single-Nucleus RNA Sequencing Data**

1590 ***Sequence alignment***

1591 All samples were processed using Cell Ranger (v5.0.0)[81]. All processing was done by using
1592 Cell Ranger's implementation of STAR to align sample sequence reads to their pre-built mm10
1593 vm23/Ens98 reference transcriptome index 2020-A, with predicted and non-validated transcripts
1594 removed. All sequencing reads were aligned to both the exons and the introns present in the
1595 index. Samples were demultiplexed to produce a pair of FASTQ files for each sample. FASTQ
1596 files containing raw read sequence information were aligned to the Cell Ranger index using the
1597 cellranger count command with --chemistry SC3Pv3 and --include-introns flags enabled. Cell
1598 Ranger corrected sequencing errors in cell barcodes to pre-defined sequences in the 10X v3
1599 single-index whitelist within Hamming distance 1. PCR duplicates were removed by selecting
1600 unique combinations of corrected cell barcodes, unique molecular identifiers, gene names, and
1601 location within the transcript. Raw unfiltered count data was read into R (v4.2.1) using the
1602 Seurat package (v4.2.0)[82]. The final result of the pipeline was a barcode x gene expression
1603 matrix for further analysis downstream.

1604 ***Quality control***

1605 We used the raw, unfiltered matrix output from Cell Ranger as the input to the beginning of the
1606 pipeline. However, to apply a more stringent filter, the emptyDrops dirichlet-multinomial model
1607 from the DropletUtils package (v1.10.2) was applied to each library individually. Droplets with
1608 less than 100 total counts were used to construct the ambient RNA profile and an FDR
1609 threshold below 0.001 was used to select putatively occupied droplets. All barcodes with greater
1610 than 1000 UMIs were further assumed non-empty. Most quality filtration choices were heavily
1611 influenced by the recommendations presented in pipeComp[83]. All quality control was
1612 performed on each library individually prior to merging. Minimal quality filtering for each barcode
1613 was performed by setting a floor of 1000 features per barcode for downstream inclusion to
1614 ensure the dataset is entirely composed of high-quality nuclei. Next, to remove highly likely
1615 multiplet barcodes, barcodes were filtered out if their count depth was more than 5 median
1616 absolute deviations above the median count depth. Barcodes were then removed if their
1617 proportion of ribosomal or mitochondrial reads was more than 5 interquartile ranges above the
1618 75th percentile (median absolute deviations cannot be used, because in many cases the
1619 median absolute deviation is 0). Heterotypic doublets were identified by creating simulated

artificial doublets in scDblFinder (v1.4.1), which uses a DoubletFinder-like model to remove barcodes similar to simulated doublets, with an assumed doublet rate of 1% per 1000 nuclei in the library[84]. Scater (v1.18.3) was used to produce initial diagnostic tSNE and UMAP plots for visually checking the influence of each above metric on the structure of the data[85].

Data processing/transformation

All datasets (initially for all nuclei and again for selected subclusters) were formatted into Seurat objects (v4.0.0), merged, and then normalized and transformed individually using the SCTransform (v2) variance stabilizing transform, which performs best according to prior comparisons in pipeComp[83]. Following the merge, all genes expressed in 3 or fewer nuclei of interest were removed from analysis. SCTransform was run returning Pearson residuals regressing out mitochondrial gene expression, retaining the top 5000 highly variable features. Dimensionality of the dataset was first reduced using principal component analysis, as implemented in Seurat's RunPCA function, retaining the top 50 principal components. Principal components were selected for downstream use by using the lower value of either the number of principal components where the lowest contributes 5% of standard deviation and all cumulatively contribute 90% of the standard deviation, or the number of principal components where the percent change in variation between the consecutive components is lower than 0.1%. These principal components were used as input to the non-linear tSNE and UMAP dimensionality reduction methods as implemented by Seurat's RunTSNE and/or RunUMAP functions with 1000 epochs at 0.5 minimum distance, with otherwise default settings.

Clusters were identified via Leiden clustering in latent space using the previously selected principal components as input. Optimal clustering resolution was identified in a supervised manner using clustree, finding the highest resolution for each dataset where clustering remains stable[86]. Cluster annotation was performed in a semi-hierarchical semi-supervised manner, where known marker genes were first used to separate all nuclei into neuronal and non-neuronal cell types, and then these cells were re-analyzed and neurons were respectively separated into glutamatergic and GABAergic neurons, while non-neuronal cells were separated into astrocytes, microglia, macrophages, oligodendrocytes and their precursors/lineage, mural cells, endothelia, and vascular leptomeningeal cells. This lower level of cells was then reanalyzed, and novel cell types were then identified within these more-granular known cell types. For identification of known cell types, clusters expressing the same marker genes were manually merged to ensure all cells of a known type were analyzed together, which did not occur for novel cell type identification. Clusters resulting from specific difference in nuclei quality instead of true changes in gene expression (i.e. markedly lower mean UMI/features per nucleus, increased ribosomal/mitochondrial gene expression proportion) were removed prior to final clustering. Relationships between cell type proportion and plCoA zone were quantitated using propeller, treating each library as an independent replicate[87].

Differential expression

Marker genes were identified using Wilcoxon rank-sum test as implemented by the FindConservedMarkers function in Seurat, using the region as a grouping variable. Genes were

accepted as differentially expressed with a minimum proportion cutoff at 0.1 and minimum fold change at 1.5-fold (log2-fold change of 0.585), with a p-value cutoff of 0.01 after Bonferroni correction. To identify genes differentially expressed by region, single-cell values were converted to pseudo-bulk by batch using the run_de function as implemented in the Libra package (v1.0.0) using default settings with a minimum proportion cutoff at 0.1, and tested for differential expression using edgeR's likelihood ratio test. Zone-specific gene expression was identified by comparing batches from the two isolated zones.

Analysis of Spatial Transcriptomics Data

Sequence and image alignment

All samples were processed using Space Ranger (v1.3.0). All processing was done by using Space Ranger's implementation of STAR to align sample sequence reads to their pre-built mm10 vm23/Ens98 reference transcriptome index 2020-A, with predicted and non-validated transcripts removed, as in snRNA-seq data alignment. Samples were demultiplexed to produce a pair of FASTQ files for each sample. FASTQ files containing raw read sequence information were aligned to the index using the spaceranger count command. Space Ranger corrected sequencing errors in cell barcodes to pre-defined sequences in the single-index whitelist within Hamming distance 1. PCR duplicates were removed by selecting unique combinations of corrected cell barcodes, unique molecular identifiers, gene names, and location within the transcript. Imaging data was processed using automatic fiducial alignment and tissue detection on a brightfield input.

Data processing/transformation

We used the image-filtered matrix output from Space Ranger as the input to the beginning of the pipeline. In a similar manner to snRNA-seq data, all datasets were formatted into Seurat objects (v5.0.0), merged, and then normalized and transformed using the SCTransform (v2) variance stabilizing transform. SCTransform was run returning Pearson residuals regressing out mitochondrial gene expression, retaining the top 5000 highly variable features. Dimensionality of the dataset was first reduced using principal component analysis, as implemented in Seurat's RunPCA function, retaining the top 50 principal components, all of which were used in downstream processing. These principal components were used as input to the non-linear tSNE and UMAP dimensionality reduction methods as implemented by Seurat's RunTSNE and/or RunUMAP functions with 1000 epochs at 0.2 minimum distance, with otherwise default settings. Clusters were identified via Leiden clustering in latent space using all 50 principal components as input. Optimal clustering resolution was identified in a supervised manner using clustree, finding the highest resolution for each dataset where clustering remains stable, choosing a resolution of 0.7. Cluster annotation was performed in a semi-supervised manner, observing where in captured plCoA regions each cluster's spots localized to. For clusters that could not be annotated from spatial location alone (e.g. OLG), marker genes were examined to determine the molecular identity of relevant spots. Spatial data was projected onto neuronal molecular cell types from snRNA-seq data and cell type likelihood was predicted using Seurat's FindTransferAnchors and TransferData functions using snRNA-seq data as a reference and

plCoA spatial data as the query, using all 50 PCs. Prediction of a minority of subtypes failed, likely due to low abundance in tissue and/or due to mediolateral spatial differences, alluded to in a separate study, causing the section not to intersect with the part of the tissue containing the relevant neuronal subtypes. Glutamatergic and GABAergic molecular subtype likelihoods were predicted separately to remove noise and increase modeled prediction confidence.

Histological Image Analysis

Registration and localization

Histology for all animals and samples was examined prior to inclusion. Localization within the coronal plane was determined by registering the coronal slice to the Allen Brain Atlas via the ABBA plugin, using elastix to sequentially perform affine and spline registration of the DAPI channel of the slice to the Nissl channel of the atlas. The region of interest was then compared to the Paxinos and Franklin atlas to confirm localization, and find the region's anteroposterior distance from bregma. This combined method was used because sections cannot be accurately registered to the Paxinos and Franklin atlas due to low Z-resolution, while the Allen Brain Atlas lacks information about anteroposterior distance from bregma. Exclusion based on histology would occur when most of the intervention fell outside of the region of interest. Due to these differences, individual representative images use the individually registered Allen Reference Atlas schematics with the comparable Paxinos and Franklin anteroposterior coordinates noted, while consolidated targeting schematics use the Paxinos and Franklin atlas for visualization.

Quantification of histological fluorescence

In anterograde tracing experiments, output quantification was performed based on background-corrected total fluorescence. For all non-collateralization anterograde experiments, fluorescence intensities were quantified using FIJI (v2.9.0) throughout the whole brain in a series of evenly-space 50 µm coronal sections, manually segmenting by region with all settings held constant within experiments. For collateralization experiments, we exclusively examined fluorescence in the MeA and NAc. We calculated background-corrected total fluorescence using the equation $F_{total} = ID - (Area \times F_{background})$, where F_{total} is the background-corrected total fluorescence, ID is the integrated density, and $F_{background}$ is the mean background fluorescence measured from four randomly selected areas per section not receiving input from plCoA. Overall proportion was calculated by taking the sum of background-corrected fluorescence values across all sections for a given region and dividing it by the sum of all background-corrected values. For retrograde experiments, we quantified number of cells using the Cell Counter plugin (v3.0.0) in FIJI. The sagittal brain slices containing the plCoA were then compared to Paxinos and Franklin, 5th Edition to count the number of cells found per distance away from bregma from -1.3 to -2.5 mm in increments of 100 µm. At least two sections per region per animal were analyzed. Representative images were produced from slide scanner image output, with background subtraction and uniform brightness and contrast thresholds applied equally to all fluorescent channels in FIJI to avoid potential distortion of visible fluorescence levels.

Quantification and analysis of RNAscope images

1739 RNAscope images were analyzed as previously described.[86] Images were opened in FIJI and
1740 individual Z-planes encompassing the entire ROI were selected from each image for further
1741 image processing. Background was subtracted from all channels in all images using the
1742 subtract background feature. Masks of each region were drawn based on the mouse brain atlas,
1743 and images were then saved as 8bit TIFFs for further cell and puncta identification in
1744 CellProfiler (v4.2.4)[88]. Image TIFFs were run through CellProfiler using an optimized version
1745 of the CellProfiler Colocalization pipeline. The pipeline was optimized to identify DAPI labelled
1746 cells (15-45 pixels in diameter) and then subsequently identify mRNA puncta (4-10 pixels in
1747 diameter). DAPI cell detection was further restricted by shrinking DAPI ROIs by 1 pixel. Puncta
1748 overlapping with DAPI-identified cells (using the relate objects module) were considered for
1749 analysis to assess the level of mRNA expression per cell. To determine if cells were expressing
1750 mRNA, a threshold of 5 or more puncta within twice the diameter of nucleus centered over the
1751 nucleus was used. Total number and density of *VGluT2*+ and *VGluT1*+ cells in each region of
1752 interest were calculated from CellProfiler .csv outputs using custom R scripts.

1753 **References**

1754 1. Stowers, L., P. Cameron, and J.A. Keller, *Ominous odors: olfactory control of instinctive*
1755 *fear and aggression in mice.* Curr Opin Neurobiol, 2013. **23**(3): p. 339-45.
1756 2. Li, Q. and S.D. Liberles, *Aversion and Attraction through Olfaction.* Current Biology,
1757 2015. **25**(3): p. R120-R129.
1758 3. Hayden, S., et al., *Ecological adaptation determines functional mammalian olfactory*
1759 *subgenomes.* Genome Research, 2010. **20**(1): p. 1-9.
1760 4. Saraiva, L.R., et al., *A transcriptomic atlas of mammalian olfactory mucosae reveals an*
1761 *evolutionary influence on food odor detection in humans.* Science Advances, 2019. **5**(7):
1762 p. eaax0396.
1763 5. Ibarra-Soria, X., et al., *Variation in olfactory neuron repertoires is genetically controlled*
1764 *and environmentally modulated.* eLife, 2017. **6**: p. e21476.
1765 6. Yeshurun, Y. and N. Sobel, *An odor is not worth a thousand words: from*
1766 *multidimensional odors to unidimensional odor objects.* Annu Rev Psychol, 2010. **61**: p.
1767 219-41, C1-5.
1768 7. Tye, K.M., *Neural Circuit Motifs in Valence Processing.* Neuron, 2018. **100**(2): p. 436-
1769 452.
1770 8. Dewan, A., et al., *Non-redundant coding of aversive odours in the main olfactory*
1771 *pathway.* Nature, 2013. **497**(7450): p. 486-489.
1772 9. Saito, H., et al., *Immobility responses are induced by photoactivation of single*
1773 *glomerular species responsive to fox odour TMT.* Nature Communications, 2017. **8**(1): p.
1774 1-10.
1775 10. Semmelhack, J.L. and J.W. Wang, *Select Drosophila glomeruli mediate innate olfactory*
1776 *attraction and aversion.* Nature, 2009. **459**(7244): p. 218-23.
1777 11. Beyeler, A., et al., *Organization of Valence-Encoding and Projection-Defined Neurons in*
1778 *the Basolateral Amygdala.* Cell Reports, 2018. **22**(4): p. 905-918.
1779 12. Sosulski, D.L., et al., *Distinct representations of olfactory information in different*
1780 *cortical centres.* Nature, 2011. **472**(7342): p. 213-219.
1781 13. Miyamichi, K., et al., *Cortical representations of olfactory input by trans-synaptic*
1782 *tracing.* Nature, 2011. **472**(7342): p. 191-199.
1783 14. Root, C.M., C.A. Denny, R. Hen, and R. Axel, *The participation of cortical amygdala in*
1784 *innate, odour-driven behaviour.* Nature, 2014. **515**(7526): p. 269-273.
1785 15. Iurilli, G. and S.R. Datta, *Population Coding in an Innately Relevant Olfactory Area.*
1786 Neuron, 2017. **93**(5): p. 1180-1197 e7.
1787 16. Tsuji, T., et al., *Coding of odors in the anterior olfactory nucleus.* Physiological Reports,
1788 2019. **7**(22): p. e14284.
1789 17. Malnic, B., J. Hirono, T. Sato, and L.B. Buck, *Combinatorial receptor codes for odors.*
1790 Cell, 1999. **96**(5): p. 713-23.
1791 18. Stettler, D.D. and R. Axel, *Representations of odor in the piriform cortex.* Neuron, 2009.
1792 **63**(6): p. 854-64.
1793 19. Soucy, E.R., et al., *Precision and diversity in an odor map on the olfactory bulb.* Nature
1794 Neuroscience, 2009. **12**(2): p. 210-220.
1795 20. Lee, D., L. Liu, and C.M. Root, *Transformation of value signaling in a striatopallidal*
1796 *circuit.* eLife, 2023. **12**.

1797 21. Cousens, G.A., *Characterization of odor-evoked neural activity in the olfactory peduncle.*
1798 IBRO Reports, 2020. **9**: p. 157-163.
1799 22. Kim, J., et al., *Antagonistic negative and positive neurons of the basolateral amygdala.*
1800 Nat Neurosci, 2016. **19**(12): p. 1636-1646.
1801 23. Root, C.M., C.A. Denny, R. Hen, and R. Axel, *The participation of cortical amygdala in*
1802 *innate, odour-driven behaviour.* Nature, 2014. **515**(7526): p. 269-73.
1803 24. Chen, X., et al., *A Gustotopic Map of Taste Qualities in the Mammalian Brain.* Science
1804 (New York, N.Y.), 2011. **333**(6047): p. 1262-1266.
1805 25. Kobayakawa, K., et al., *Innate versus learned odour processing in the mouse olfactory*
1806 *bulb.* Nature, 2007. **450**(7169): p. 503-8.
1807 26. Wang, L., et al., *The coding of valence and identity in the mammalian taste system.*
1808 Nature, 2018. **558**(7708): p. 127-131.
1809 27. Boyden, E.S., et al., *Millisecond-timescale, genetically targeted optical control of neural*
1810 *activity.* Nat Neurosci, 2005. **8**(9): p. 1263-8.
1811 28. Tasic, B., et al., *Adult mouse cortical cell taxonomy revealed by single cell*
1812 *transcriptomics.* Nat Neurosci, 2016. **19**(2): p. 335-46.
1813 29. Zeisel, A., et al., *Molecular Architecture of the Mouse Nervous System.* Cell, 2018.
1814 **174**(4): p. 999-1014 e22.
1815 30. Marques, S., et al., *Oligodendrocyte heterogeneity in the mouse juvenile and adult*
1816 *central nervous system.* Science (New York, N.Y.), 2016. **352**(6291): p. 1326-1329.
1817 31. Yasuda, K., et al., *Drug Transporters on Arachnoid Barrier Cells Contribute to the*
1818 *Blood–Cerebrospinal Fluid Barrier.* Drug Metabolism and Disposition, 2013. **41**(4): p.
1819 923-931.
1820 32. Tasic, B., et al., *Shared and distinct transcriptomic cell types across neocortical areas.*
1821 Nature, 2018. **563**(7729): p. 72-78.
1822 33. Yao, Z., et al., *A taxonomy of transcriptomic cell types across the isocortex and*
1823 *hippocampal formation.* Cell, 2021. **184**(12): p. 3222.
1824 34. Armbruster, B.N., et al., *Evolving the lock to fit the key to create a family of G protein-*
1825 *coupled receptors potently activated by an inert ligand.* Proc Natl Acad Sci U S A, 2007.
1826 **104**(12): p. 5163-8.
1827 35. Muller, M. and M. Fendt, *Temporary inactivation of the medial and basolateral*
1828 *amygdala differentially affects TMT-induced fear behavior in rats.* Behav Brain Res,
1829 2006. **167**(1): p. 57-62.
1830 36. Ikemoto, S., *Dopamine reward circuitry: two projection systems from the ventral*
1831 *midbrain to the nucleus accumbens-olfactory tubercle complex.* Brain Research Reviews,
1832 2007. **56**(1): p. 27-78.
1833 37. Kaas, J.H., *Topographic maps are fundamental to sensory processing.* Brain Res Bull,
1834 1997. **44**(2): p. 107-12.
1835 38. Garrett, M.E., I. Nauhaus, J.H. Marshel, and E.M. Callaway, *Topography and Areal*
1836 *Organization of Mouse Visual Cortex.* Journal of Neuroscience, 2014. **34**(37): p. 12587-
1837 12600.
1838 39. Kaas, J.H., et al., *Multiple Representations of the Body Within the Primary*
1839 *Somatosensory Cortex of Primates.* Science, 1979. **204**(4392): p. 521-523.
1840 40. Schreiner, C.E. and J.A. Winer, *Auditory Cortex Mapmaking: Principles, Projections,*
1841 *and Plasticity.* Neuron, 2007. **56**(2): p. 356-365.

41. Miyamichi, K., et al., *Cortical representations of olfactory input by trans-synaptic tracing.* Nature, 2011. **472**(7342): p. 191-6.
42. Wang, I.H., et al., *Spatial transcriptomic reconstruction of the mouse olfactory glomerular map suggests principles of odor processing.* Nature Neuroscience, 2022. **25**(4): p. 484-492.
43. Ressler, K.J., S.L. Sullivan, and L.B. Buck, *A zonal organization of odorant receptor gene expression in the olfactory epithelium.* Cell, 1993. **73**(3): p. 597-609.
44. Zapiec, B. and P. Mombaerts, *The Zonal Organization of Odorant Receptor Gene Choice in the Main Olfactory Epithelium of the Mouse.* Cell Reports, 2020. **30**(12): p. 4220-4234.e5.
45. Kermen, F., et al., *Topographical representation of odor hedonics in the olfactory bulb.* Nature Neuroscience, 2016. **19**(7): p. 876-878.
46. Choi, G.B., et al., *Lhx6 Delineates a Pathway Mediating Innate Reproductive Behaviors from the Amygdala to the Hypothalamus.* Neuron, 2005. **46**(4): p. 647-660.
47. Cohn, R., I. Morantte, and V. Ruta, *Coordinated and Compartmentalized Neuromodulation Shapes Sensory Processing in Drosophila.* Cell, 2015. **163**(7): p. 1742-1755.
48. Chen, K., J.F. Kogan, and A. Fontanini, *Spatially Distributed Representation of Taste Quality in the Gustatory Insular Cortex of Behaving Mice.* Current Biology, 2021. **31**(2): p. 247-256.e4.
49. Erö, C., M.-O. Gewaltig, D. Keller, and H. Markram, *A Cell Atlas for the Mouse Brain.* Frontiers in Neuroinformatics, 2018. **12**.
50. Cembrowski, M.S., et al., *Dissociable Structural and Functional Hippocampal Outputs via Distinct Subiculum Cell Classes.* Cell, 2018. **173**(5): p. 1280-1292.e18.
51. Cembrowski, M.S. and N. Spruston, *Heterogeneity within classical cell types is the rule: lessons from hippocampal pyramidal neurons.* Nature Reviews Neuroscience, 2019. **20**(4): p. 193-204.
52. Scala, F., et al., *Phenotypic variation of transcriptomic cell types in mouse motor cortex.* Nature, 2021. **598**(7879): p. 144-150.
53. Calvigioni, D., et al., *Esr1+ hypothalamic-habenula neurons shape aversive states.* Nature Neuroscience, 2023. **26**(7): p. 1245-1255.
54. Phillips, J.W., et al., *A repeated molecular architecture across thalamic pathways.* Nature neuroscience, 2019. **22**(11): p. 1925.
55. Mandelbaum, G., et al., *Distinct Cortical-Thalamic-Striatal Circuits through the Parafascicular Nucleus.* Neuron, 2019. **102**(3): p. 636-652.e7.
56. Hochgerner, H., et al., *Neuronal types in the mouse amygdala and their transcriptional response to fear conditioning.* Nature Neuroscience, 2023. **26**(12): p. 2237-2249.
57. Klingler, E., *Development and Organization of the Evolutionarily Conserved Three-Layered Olfactory Cortex.* eNeuro, 2017. **4**(1).
58. Shi, H., et al., *Spatial atlas of the mouse central nervous system at molecular resolution.* Nature, 2023. **622**(7983): p. 552-561.
59. Yao, Z., et al., *A high-resolution transcriptomic and spatial atlas of cell types in the whole mouse brain.* Nature, 2023. **624**(7991): p. 317-332.
60. Zhang, M., et al., *Molecularly defined and spatially resolved cell atlas of the whole mouse brain.* Nature, 2023. **624**(7991): p. 343-354.

1887 61. Mills, F., et al., *Amygdalostriatal transition zone neurons encode sustained valence to*
1888 *direct conditioned behaviors*. 2022, bioRxiv.
1889 62. Singer, W., *Recurrent dynamics in the cerebral cortex: Integration of sensory evidence*
1890 *with stored knowledge.* Proceedings of the National Academy of Sciences, 2021. **118**(33):
1891 p. e2101043118.
1892 63. Floresco, S.B., *The Nucleus Accumbens: An Interface Between Cognition, Emotion, and*
1893 *Action.* https://doi.org/10.1146/annurev-psych-010213-115159, 2015.
1894 64. Day, H.E., C.V. Masini, and S. Campeau, *The pattern of brain c-fos mRNA induced by a*
1895 *component of fox odor, 2,5-dihydro-2,4,5-trimethylthiazoline (TMT), in rats, suggests*
1896 *both systemic and processive stress characteristics.* Brain Res, 2004. **1025**(1-2): p. 139-
1897 51.
1898 65. Zador, A.M., *A critique of pure learning and what artificial neural networks can learn*
1899 *from animal brains.* Nature Communications, 2019. **10**(1): p. 3770.
1900 66. Koulakov, A., S. Shuvaev, D. Lachi, and A. Zador, *Encoding innate ability through a*
1901 *genomic bottleneck*. 2022, bioRxiv.
1902 67. Barabási, D.L., T. Beynon, Á. Katona, and N. Perez-Nieves, *Complex computation from*
1903 *developmental priors.* Nature Communications, 2023. **14**: p. 2226.
1904 68. Chae, H., et al., *Mosaic representations of odors in the input and output layers of the*
1905 *mouse olfactory bulb.* Nature Neuroscience, 2019. **22**(8): p. 1306-1317.
1906 69. Martiros, N., V. Kapoor, S.E. Kim, and V.N. Murthy, *Distinct representation of cue-*
1907 *outcome association by D1 and D2 neurons in the ventral striatum's olfactory tubercle.*
1908 eLife, 2022. **11**: p. e75463.
1909 70. Qiu, Q., Y. Wu, L. Ma, and C.R. Yu, *Encoding innately recognized odors via a*
1910 *generalized population code.* Current Biology, 2021. **31**(9): p. 1813-1825.e4.
1911 71. Nair, A., et al., *An approximate line attractor in the hypothalamus encodes an aggressive*
1912 *state.* Cell, 2023. **186**(1): p. 178-193 e15.
1913 72. Wang, Y., et al., *Large-scale forward genetics screening identifies Trpa1 as a*
1914 *chemosensor for predator odor-evoked innate fear behaviors.* Nat Commun, 2018. **9**(1):
1915 p. 2041.
1916 73. Hacquemand, R., L. Jacquot, and G. Brand, *Comparative Fear-Related Behaviors to*
1917 *Predator Odors (TMT and Natural Fox Feces) before and after Intranasal ZnSO(4)*
1918 *Treatment in Mice.* Front Behav Neurosci, 2010. **4**: p. 188.
1919 74. Ayers, L.W., A. Asok, F.D. Heyward, and J.B. Rosen, *Freezing to the predator odor*
1920 *2,4,5 dihydro 2,5 trimethylthiazoline (TMT) is disrupted by olfactory bulb removal but*
1921 *not trigeminal deafferentation.* Behav Brain Res, 2013. **253**: p. 54-9.
1922 75. Davis, A., R. Gao, and N.E. Navin, *SCOPIT: sample size calculations for single-cell*
1923 *sequencing experiments.* BMC Bioinformatics, 2019. **20**(1): p. 566.
1924 76. Sturchler-Pierrat, C., et al., *Two amyloid precursor protein transgenic mouse models with*
1925 *Alzheimer disease-like pathology.* Proceedings of the National Academy of Sciences,
1926 1997. **94**(24): p. 13287-13292.
1927 77. Preissl, S., et al., *Single-nucleus analysis of accessible chromatin in developing mouse*
1928 *forebrain reveals cell-type-specific transcriptional regulation.* Nat Neurosci, 2018. **21**(3):
1929 p. 432-439.
1930 78. Krishnaswami, S.R., et al., *Using single nuclei for RNA-seq to capture the transcriptome*
1931 *of postmortem neurons.* Nat Protoc, 2016. **11**(3): p. 499-524.

1932 79. Pnevmatikakis, E.A. and A. Giovannucci, *NoRMCorre: An online algorithm for*
1933 *piecewise rigid motion correction of calcium imaging data.* Journal of Neuroscience
1934 Methods, 2017. **291**: p. 83-94.
1935 80. Pnevmatikakis, E.A., et al., *Simultaneous Denoising, Deconvolution, and Demixing of*
1936 *Calcium Imaging Data.* Neuron, 2016. **89**(2): p. 285-299.
1937 81. Zheng, G.X., et al., *Massively parallel digital transcriptional profiling of single cells.* Nat
1938 Commun, 2017. **8**: p. 14049.
1939 82. Butler, A., et al., *Integrating single-cell transcriptomic data across different conditions,*
1940 *technologies, and species.* Nature Biotechnology, 2018. **36**(5): p. 411-420.
1941 83. Germain, P.-L., A. Sonrel, and M.D. Robinson, *pipeComp, a general framework for the*
1942 *evaluation of computational pipelines, reveals performant single cell RNA-seq*
1943 *preprocessing tools.* Genome Biology, 2020. **21**(1): p. 227.
1944 84. McGinnis, C.S., L.M. Murrow, and Z.J. Gartner, *DoubletFinder: Doublet Detection in*
1945 *Single-Cell RNA Sequencing Data Using Artificial Nearest Neighbors.* Cell Systems,
1946 2019. **8**(4): p. 329-337.e4.
1947 85. McCarthy, D.J., et al., *Scater: pre-processing, quality control, normalization and*
1948 *visualization of single-cell RNA-seq data in R.* Bioinformatics, 2017. **33**(8): p. btw777.
1949 86. Zappia, L. and A. Oshlack, *Clustering trees: a visualization for evaluating clusterings at*
1950 *multiple resolutions.* GigaScience, 2018. **7**(7): p. giy083.
1951 87. Phipson, B., et al., *propeller: testing for differences in cell type proportions in single cell*
1952 *data.* Bioinformatics, 2022. **38**(20): p. 4720-4726.
1953 88. Carpenter, A.E., et al., *CellProfiler: image analysis software for identifying and*
1954 *quantifying cell phenotypes.* Genome Biology, 2006. **7**(10): p. R100.

1955

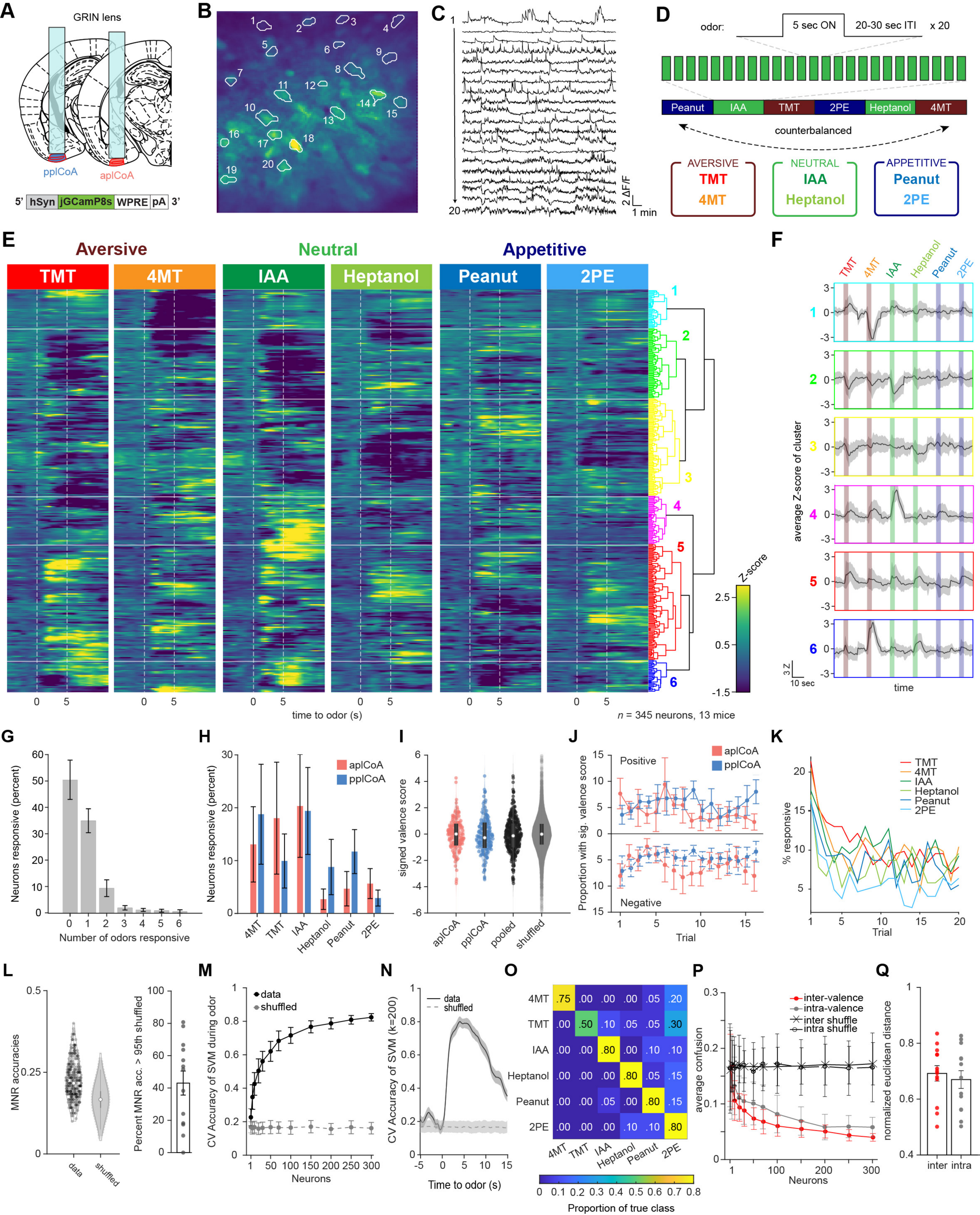
A
GRIN lens
pplCoA
aplCoA
5' hSyn jGCamP8s WPRE pA 3'
B
C
1 min
2 ΔF/F
D
odor:
5 sec ON
20-30 sec ITI
x 20
Peanut
IAA
TMT
2PE
Heptanol
4MT
counterbalanced
AVERSIVE
TMT
4MT
NEUTRAL
IAA
Heptanol
APPETITIVE
Peanut
2PE
E
Aversive
Neutral
Appetitive
TMT
4MT
IAA
Heptanol
Peanut
2PE
Z-score
time to odor (s)
n = 345 neurons, 13 mice
F
average Z-score of cluster
10 sec
time
G
Neurons responsive (percent)
Number of odors responsive
H
aplCoA
pplCoA
Neurons responsive (percent)
4MT
TMT
IAA
Heptanol
Peanut
2PE
I
signed valence score
aplCoA
pplCoA
pooled
shuffled
J
Positive
Negative
Proportion with sig. valence score
Trial
K
% responsive
Trial
L
MNR accuracies
data
shuffled
Percent MNR acc. > 95th shuffled
M
CV Accuracy of SVM during odor
Neurons
N
CV Accuracy of SVM (k=200)
Time to odor (s)
O
Proportion of true class
P
inter-valence
intra-valence
inter shuffle
intra shuffle
average confusion
Neurons
Q
normalized euclidean distance
inter
intra

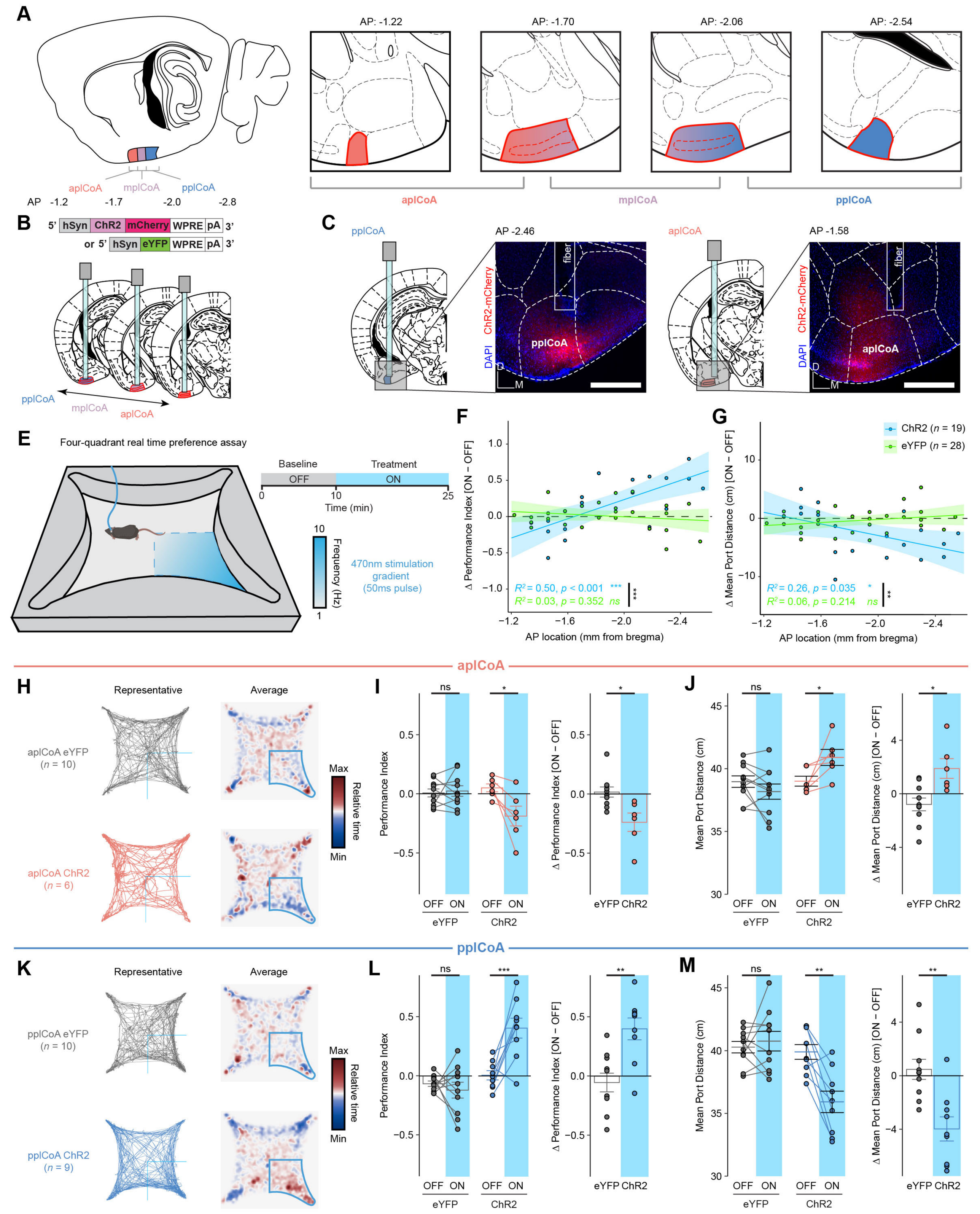
A
AP: -1.22
AP: -1.70
AP: -2.06
AP: -2.54
aplCoA
mplCoA
pplCoA
AP -1.2 -1.7 -2.0 -2.8
B
5' hSyn ChR2 mCherry WPRE pA 3'
or 5' hSyn eYFP WPRE pA 3'
pplCoA
mplCoA
aplCoA
C
pplCoA
AP -2.46
ChR2-mCherry
DAPI
fiber
D
M
aplCoA
AP -1.58
E
Four-quadrant real time preference assay
Baseline
Treatment
OFF
ON
0
10
25
Time (min)
10
1
Frequency (Hz)
470nm stimulation gradient (50ms pulse)
F
Δ Performance Index [ON – OFF]
R^2 = 0.50, p < 0.001 ***
R^2 = 0.03, p = 0.352 ns
AP location (mm from bregma)
G
ChR2 (n = 19)
eYFP (n = 28)
Δ Mean Port Distance (cm) [ON – OFF]
R^2 = 0.26, p = 0.035 *
R^2 = 0.06, p = 0.214 ns
AP location (mm from bregma)
aplCoA
H
Representative
Average
aplCoA eYFP (n = 10)
aplCoA ChR2 (n = 6)
Max
Relative time
Min
I
Performance Index
Δ Performance Index [ON – OFF]
ns
*
OFF ON
eYFP
ChR2
J
Mean Port Distance (cm)
Δ Mean Port Distance (cm) [ON – OFF]
pplCoA
K
Representative
Average
pplCoA eYFP (n = 10)
pplCoA ChR2 (n = 9)
Max
Relative time
Min
L
Performance Index
Δ Performance Index [ON – OFF]
ns
***
**
M
Mean Port Distance (cm)
Δ Mean Port Distance (cm) [ON – OFF]

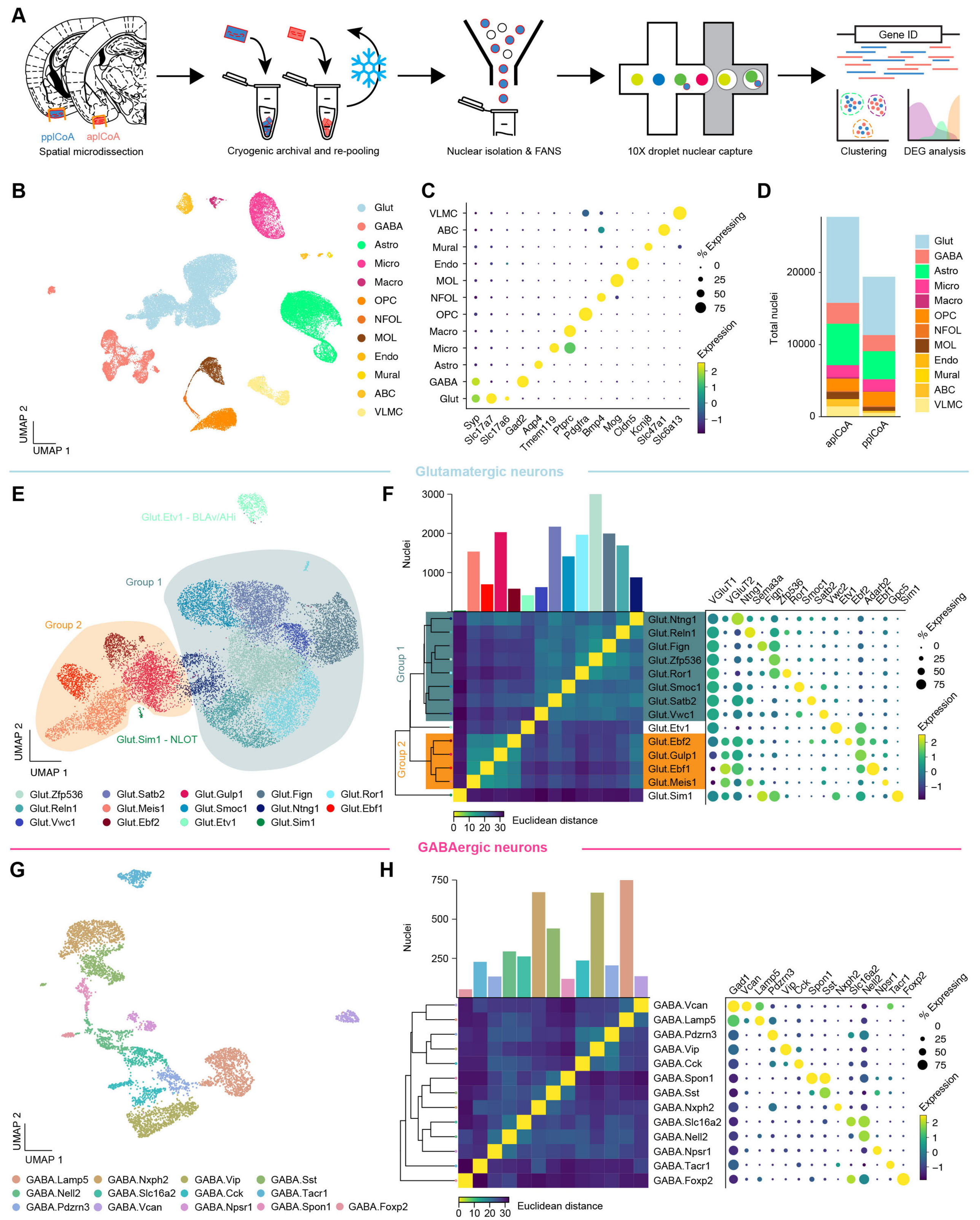
A
ppICoA
apICoA
Spatial microdissection
Cryogenic archival and re-pooling
Nuclear isolation & FANS
10X droplet nuclear capture
Gene ID
Clustering
DEG analysis
B
Glut
GABA
Astro
Micro
Macro
OPC
NFOL
MOL
Endo
Mural
ABC
VLMC
UMAP 2
UMAP 1
C
VLMC
ABC
Mural
Endo
MOL
NFOL
OPC
Macro
Micro
Astro
GABA
Glut
Syp
Slc17a7
Slc17a6
Gad2
Aqp4
Tmem119
Ptprc
Pdgfra
Bmp4
Mog
Cldn5
Kcnj8
Slc47a1
Slc6a13
% Expressing
0
25
50
75
Expression
2
1
0
−1
D
Total nuclei
20000
10000
0
apICoA
ppICoA
Glut
GABA
Astro
Micro
Macro
OPC
NFOL
MOL
Endo
Mural
ABC
VLMC
Glutamatergic neurons
E
Glut.Etv1 - BLAv/AHi
Group 1
Group 2
Glut.Sim1 - NLOT
UMAP 2
UMAP 1
Glut.Zfp536
Glut.Reln1
Glut.Vwc1
Glut.Satb2
Glut.Meis1
Glut.Ebf2
Glut.Gulp1
Glut.Smoc1
Glut.Etv1
Glut.Fign
Glut.Ntng1
Glut.Sim1
Glut.Ror1
Glut.Ebf1
F
Nuclei
3000
2000
1000
VGluT1
VGluT2
Ntng1
Sema3a
Fign
Zfp536
Ror1
Smoc1
Satb2
Vwc2
Etv1
Ebf2
Adarb2
Ebf1
Gpc5
Sim1
Glut.Ntng1
Glut.Reln1
Glut.Fign
Glut.Zfp536
Glut.Ror1
Glut.Smoc1
Glut.Satb2
Glut.Vwc1
Glut.Etv1
Glut.Ebf2
Glut.Gulp1
Glut.Ebf1
Glut.Meis1
Glut.Sim1
Group 1
Group 2
% Expressing
0
25
50
75
Expression
2
1
0
−1
0 10 20 30
Euclidean distance
GABAergic neurons
G
UMAP 2
UMAP 1
GABA.Lamp5
GABA.Nell2
GABA.Pdzrn3
GABA.Nxph2
GABA.Slc16a2
GABA.Vcan
GABA.Vip
GABA.Cck
GABA.Npsr1
GABA.Sst
GABA.Tacr1
GABA.Spon1
GABA.Foxp2
H
Nuclei
750
500
250
Gad1
Vcan
Lamp5
Pdzrn3
Vip
Cck
Spon1
Sst
Nxph2
Slc16a2
Nell2
Npsr1
Tacr1
Foxp2
GABA.Vcan
GABA.Lamp5
GABA.Pdzrn3
GABA.Vip
GABA.Cck
GABA.Spon1
GABA.Sst
GABA.Nxph2
GABA.Slc16a2
GABA.Nell2
GABA.Npsr1
GABA.Tacr1
GABA.Foxp2
% Expressing
0
25
50
75
Expression
2
1
0
−1
0 10 20 30
Euclidean distance

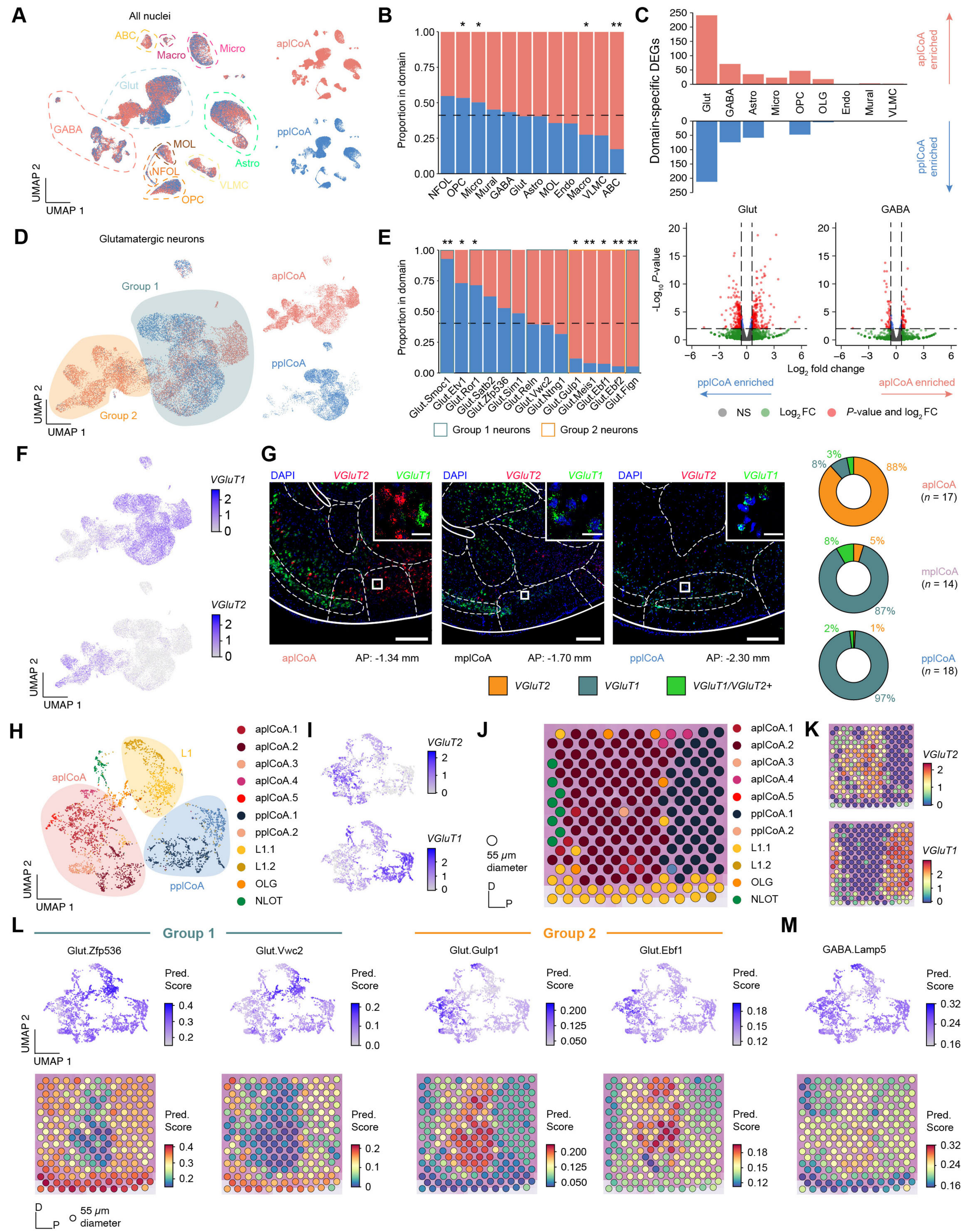
A
All nuclei
ABC
Macro
Micro
Glut
GABA
MOL
NFOL
OPC
Astro
VLMC
aplCoA
pplCoA
UMAP 2
UMAP 1
B
Proportion in domain
NFOL
OPC
Micro
Mural
GABA
Glut
Astro
MOL
Endo
Macro
VLMC
ABC
C
Domain-specific DEGs
Glut
GABA
Astro
Micro
OPC
OLG
Endo
Mural
VLMC
aplCoA enriched
pplCoA enriched
D
Glutamatergic neurons
Group 1
Group 2
aplCoA
pplCoA
E
Glut.Smoc1
Glut.Etv1
Glut.Ror1
Glut.Satb2
Glut.Zfp536
Glut.Sim1
Glut.Reln
Glut.Vwc2
Glut.Ntng1
Glut.Gulp1
Glut.Meis1
Glut.Ebf1
Glut.Ebf2
Glut.Fign
Group 1 neurons
Group 2 neurons
Glut
GABA
-Log10 P-value
Log2 fold change
pplCoA enriched
aplCoA enriched
NS
Log2 FC
P-value and log2 FC
F
VGluT1
VGluT2
G
DAPI
VGluT2
VGluT1
aplCoA
AP: -1.34 mm
mplCoA
AP: -1.70 mm
pplCoA
AP: -2.30 mm
VGluT2
VGluT1
VGluT1/VGluT2+
aplCoA (n = 17)
mplCoA (n = 14)
pplCoA (n = 18)
H
aplCoA
L1
pplCoA
aplCoA.1
aplCoA.2
aplCoA.3
aplCoA.4
aplCoA.5
pplCoA.1
pplCoA.2
L1.1
L1.2
OLG
NLOT
I
J
55 μm diameter
K
L
Group 1
Group 2
Glut.Zfp536
Glut.Vwc2
Glut.Gulp1
Glut.Ebf1
M
GABA.Lamp5
Pred. Score
55 μm diameter

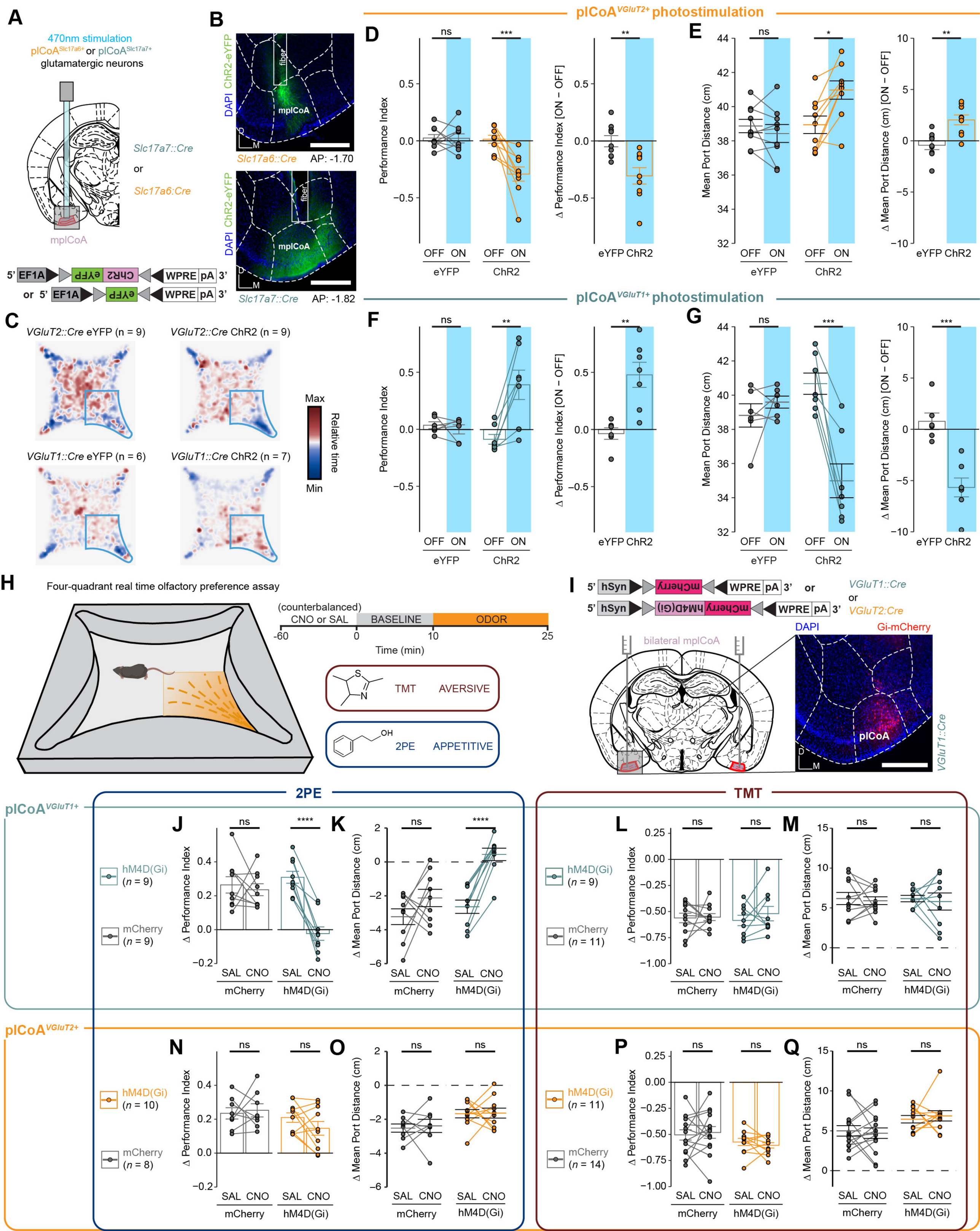
A
470nm stimulation
pICoA Slc17a6+ or pICoA Slc17a7+
glutamatergic neurons
Slc17a7::Cre
or
Slc17a6:Cre
mpICoA
5' EF1A ChR2 eYFP WPRE pA 3'
or 5' EF1A eYFP WPRE pA 3'
B
DAPI ChR2-eYFP
fiber
mpICoA
Slc17a6::Cre AP: -1.70
Slc17a7::Cre AP: -1.82
pICoA VGluT2+ photostimulation
D
E
Performance Index
Δ Performance Index [ON – OFF]
Mean Port Distance (cm)
Δ Mean Port Distance (cm) [ON – OFF]
OFF ON
eYFP ChR2
C
VGluT2::Cre eYFP (n = 9)
VGluT2::Cre ChR2 (n = 9)
VGluT1::Cre eYFP (n = 6)
VGluT1::Cre ChR2 (n = 7)
Max
Min
Relative time
pICoA VGluT1+ photostimulation
F
G
H
Four-quadrant real time olfactory preference assay
(counterbalanced)
CNO or SAL
BASELINE
ODOR
Time (min)
TMT AVERSIVE
2PE APPETITIVE
I
5' hSyn mCherry WPRE pA 3' or
5' hSyn mCherry hM4D(Gi) WPRE pA 3'
VGluT1::Cre
or
VGluT2:Cre
bilateral mpICoA
DAPI
Gi-mCherry
pICoA
2PE
TMT
pICoA VGluT1+
pICoA VGluT2+
J
K
L
M
N
O
P
Q
hM4D(Gi) (n = 9)
mCherry (n = 9)
hM4D(Gi) (n = 10)
mCherry (n = 8)
hM4D(Gi) (n = 11)
mCherry (n = 11)
mCherry (n = 14)
Δ Performance Index
Δ Mean Port Distance (cm)
SAL CNO
mCherry
hM4D(Gi)

pICoA projections

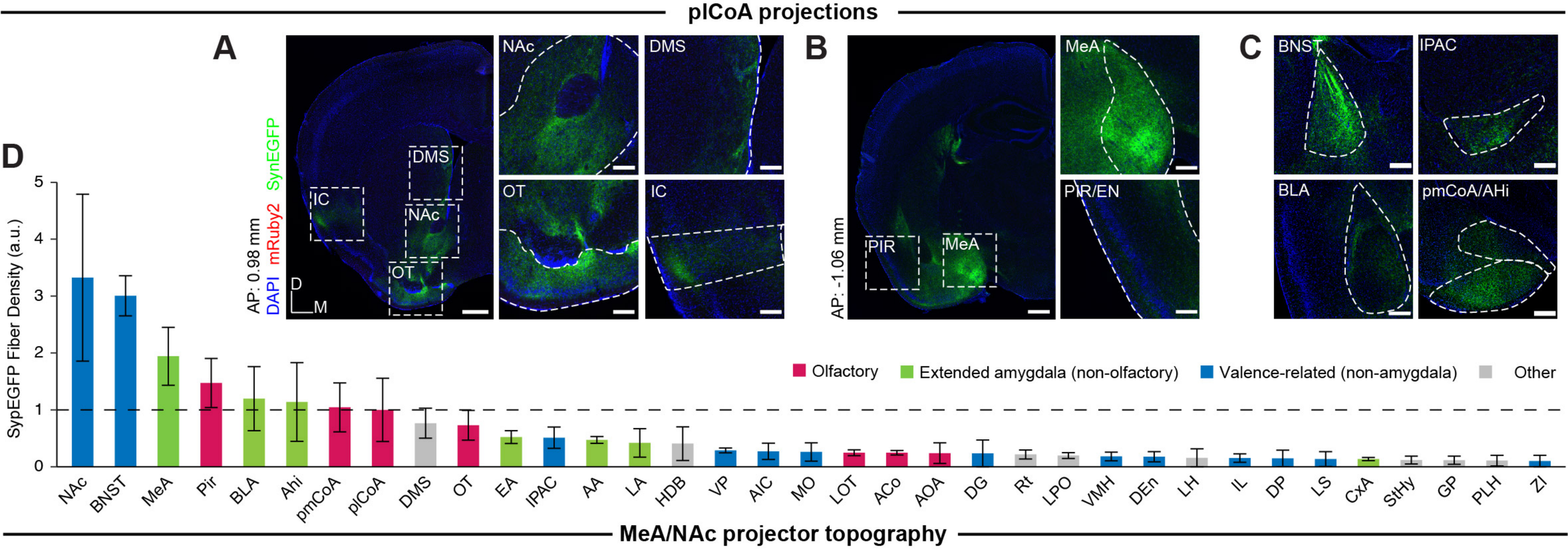

MeA/NAc projector topography

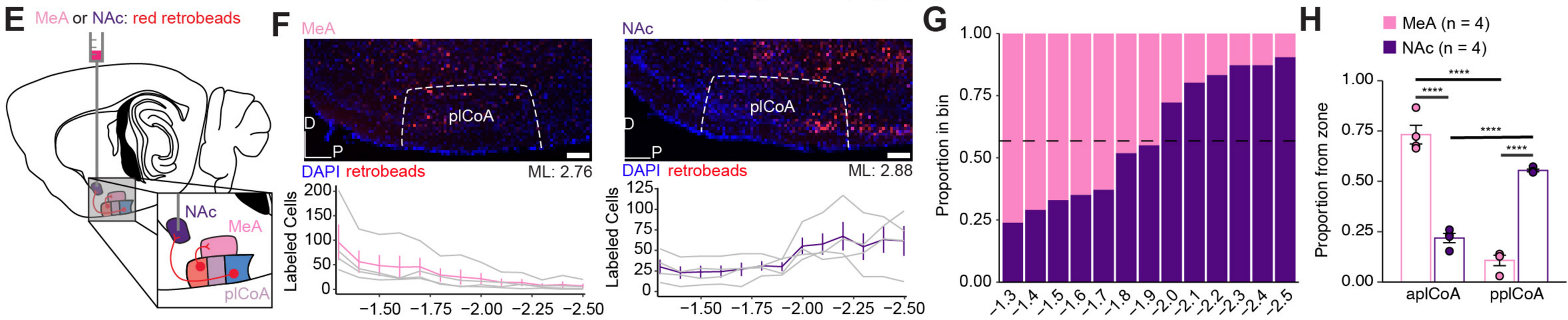

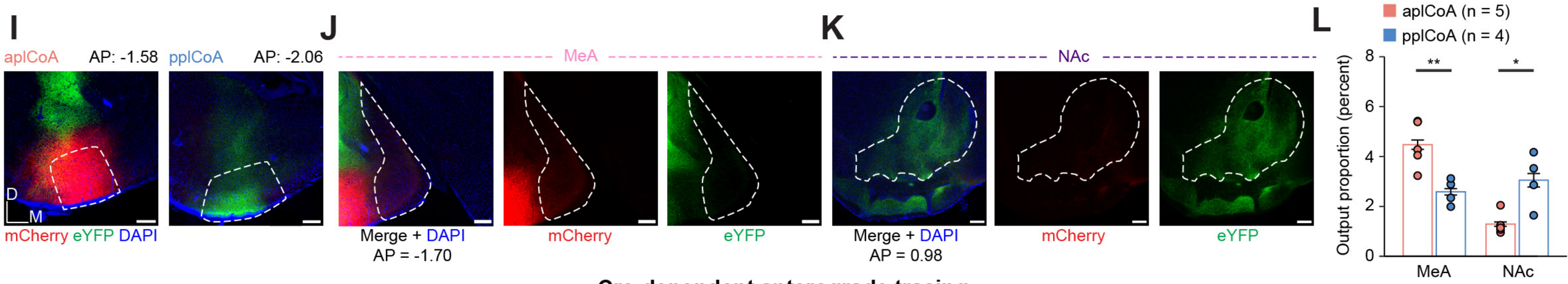

Cre-dependent anterograde tracing

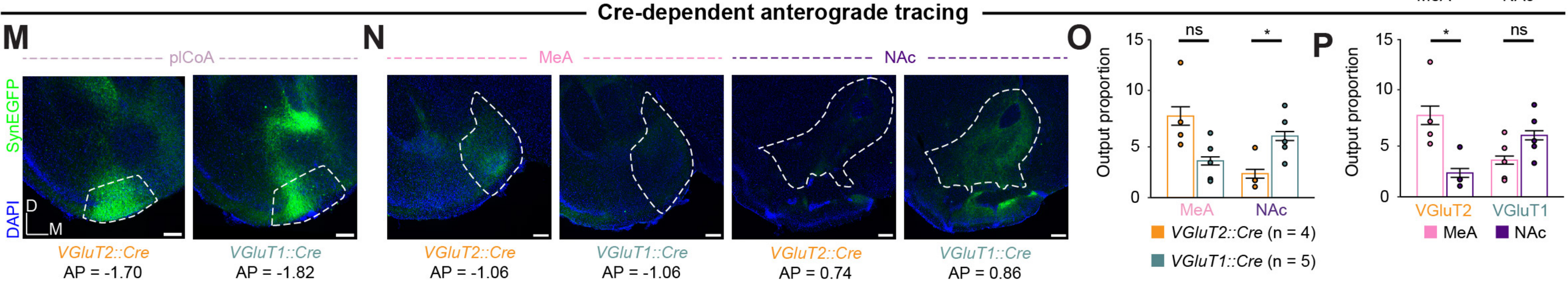

Anterograde collateralization tracing

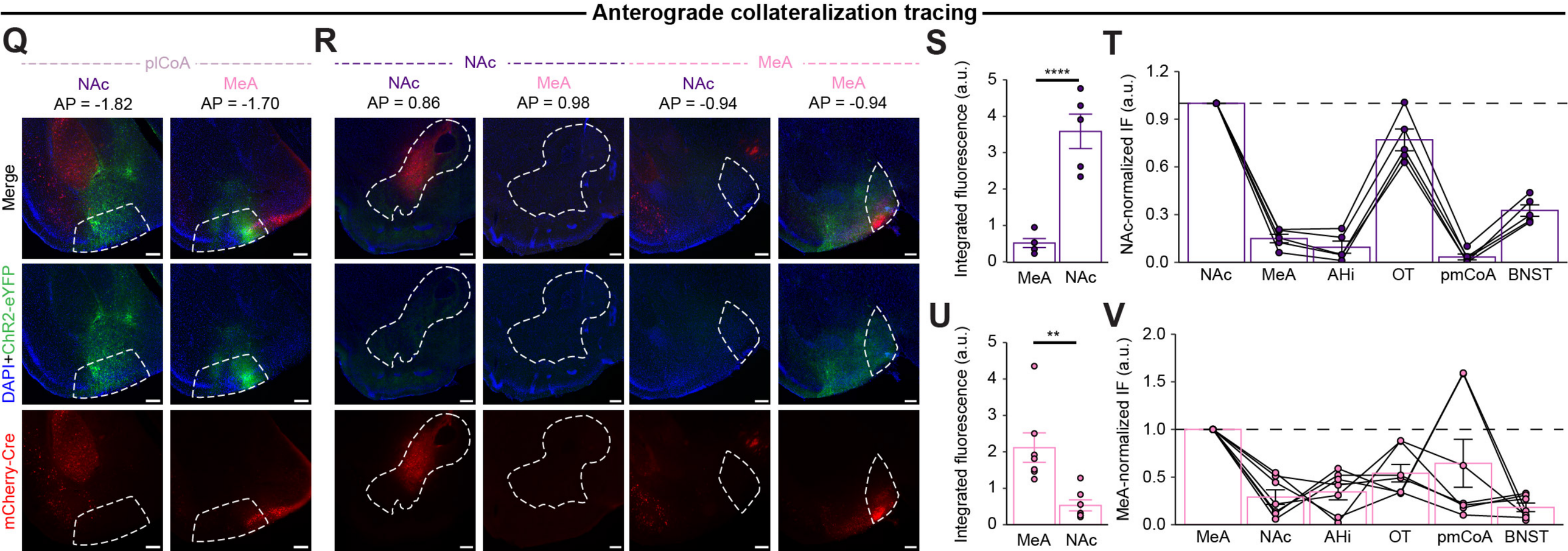

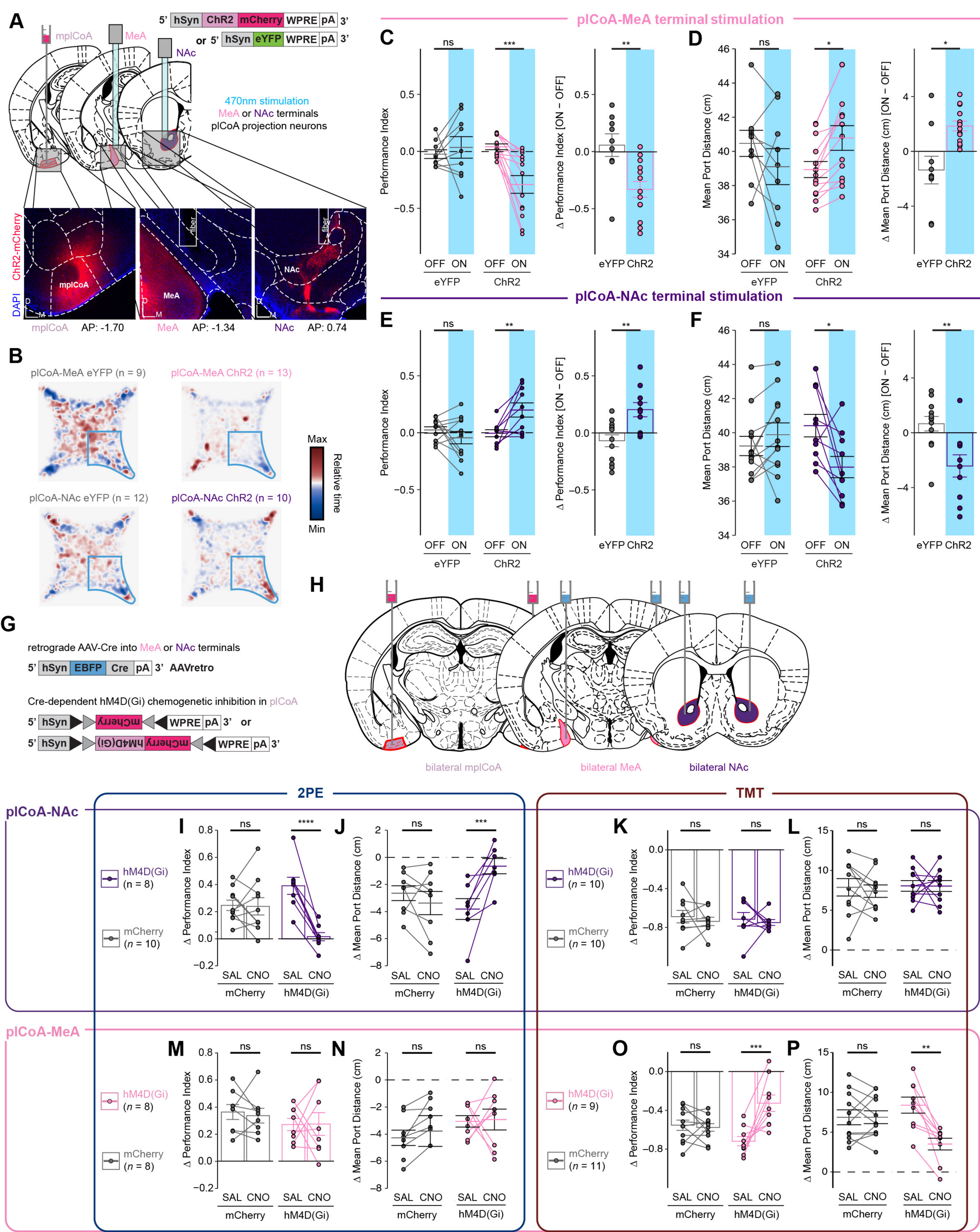
A
5' hSyn ChR2 mCherry WPRE pA 3'
or 5' hSyn eYFP WPRE pA 3'
mplCoA
MeA
NAc
470nm stimulation
MeA or NAc terminals
plCoA projection neurons
ChR2-mCherry
DAPI
mplCoA AP: -1.70
MeA AP: -1.34
NAc AP: 0.74
B
plCoA-MeA eYFP (n = 9)
plCoA-MeA ChR2 (n = 13)
plCoA-NAc eYFP (n = 12)
plCoA-NAc ChR2 (n = 10)
Max
Min
Relative time
plCoA-MeA terminal stimulation
C
D
Performance Index
Δ Performance Index [ON – OFF]
Mean Port Distance (cm)
Δ Mean Port Distance (cm) [ON – OFF]
OFF ON
eYFP
ChR2
plCoA-NAc terminal stimulation
E
F
G
retrograde AAV-Cre into MeA or NAc terminals
5' hSyn EBFP Cre pA 3' AAVretro
Cre-dependent hM4D(Gi) chemogenetic inhibition in plCoA
5' hSyn mCherry WPRE pA 3' or
5' hSyn mCherry hM4D(Gi) WPRE pA 3'
H
bilateral mplCoA
bilateral MeA
bilateral NAc
2PE
TMT
plCoA-NAc
plCoA-MeA
I
J
K
L
M
N
O
P
hM4D(Gi) (n = 8)
mCherry (n = 10)
hM4D(Gi) (n = 10)
mCherry (n = 10)
hM4D(Gi) (n = 8)
mCherry (n = 8)
hM4D(Gi) (n = 9)
mCherry (n = 11)
Δ Performance Index
Δ Mean Port Distance (cm)
SAL CNO
mCherry
hM4D(Gi)

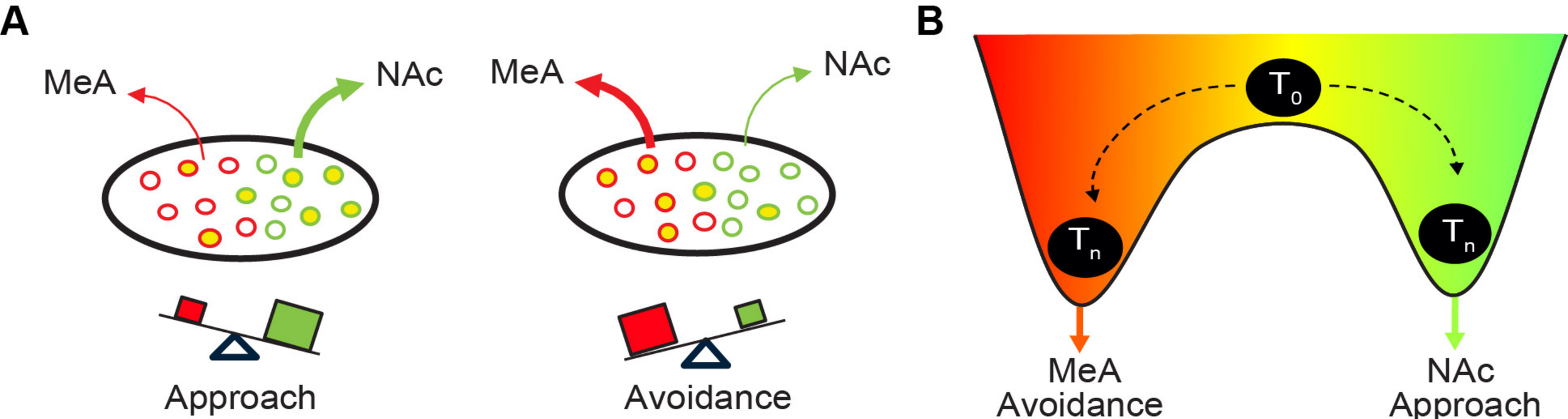
A
MeA
NAc
Approach
MeA
NAc
Avoidance
B
T_0
T_n
T_n
MeA
Avoidance
NAc
Approach